Titre: Title:	Traveling-Waves in DC-Biased Metallic Carbon Nanotubes: Theoretical Investigation of Amplification and Fabrication of Characterization Fixture
Auteur: Author:	Milad Dagher
Date:	2011
Type:	Mémoire ou thèse / Dissertation or Thesis
Référence: Citation:	Dagher, M. (2011). Traveling-Waves in DC-Biased Metallic Carbon Nanotubes: Theoretical Investigation of Amplification and Fabrication of Characterization Fixture [Mémoire de maîtrise, École Polytechnique de Montréal]. PolyPublie. https://publications.polymtl.ca/691/

URL de PolyPublie: PolyPublie URL:	https://publications.polymtl.ca/691/
Directeurs de recherche: Advisors:	Christophe Caloz, & Richard Martel
Programme: Program:	génie électrique

UNIVERSITÉ DE MONTRÉAL

TRAVELING-WAVES IN DC-BIASED METALLIC CARBON NANOTUBES: THEORETICAL INVESTIGATION OF AMPLIFICATION AND FABRICATION OF CHARACTERIZATION FIXTURE

MILAD DAGHER
DÉPARTEMENT DE GÉNIE ÉLECTRIQUE
ÉCOLE POLYTECHNIQUE DE MONTRÉAL

MÉMOIRE PRÉSENTÉ EN VUE DE L'OBTENTION
DU DIPLÔME DE MAÎTRISE ÈS SCIENCES APPLIQUÉES
(GÉNIE ÉLECTRIQUE)
OCTOBRE 2011

UNIVERSITÉ DE MONTRÉAL

ÉCOLE POLYTECHNIQUE DE MONTRÉAL

Ce mémoire intitulé :

TRAVELING-WAVES IN DC-BIASED METALLIC CARBON NANOTUBES: THEORETICAL INVESTIGATION OF AMPLIFICATION AND FABRICATION OF CHARACTERIZATION FIXTURE

présenté par : DAGHER, Milad
en vue de l'obtention du diplôme de : Maîtrise ès Sciences Appliquées
a été dûment accepté par le jury d'examen constitué de :

M. MÉNARD, David, Ph.D., président.
M. CALOZ, Christophe, Ph.D., membre et directeur de recherche.
M. MARTEL, Richard, Ph.D., membre et codirecteur de recherche.
M. SZKOPEK, Thomas, Ph.D., membre.

To Najah.

ACKNOWLEDGMENTS

First and foremost I would like thank my supervisor Prof Christophe Caloz for allowing me to work on this challenging multiphysics project which exposed me to many concepts in electromagnetics and solid-state transport. His support which he ensured to be available in a number of ways is a critical aspect that made this thesis possible, and for that I am deeply grateful. He taught me the essence of being a researcher, and how to tackle the most abstract and complex concepts by reducing them into one single and clear 'point'.

I want to also thank my co-supervisor Prof Richard Martel for his mentorship and encouragement which gave me the boost needed many times throughout the past two years. Moreover, I want to thank him for the long discussions which were always fruitful, interesting, and motivating.

I want also to thank the members of the jury, Prof David Ménard and Prof Thomas Szkopek, for considering my thesis. Their remarks, notes, and questions were of vital importance to my Masters presentation.

The theoretical part of this thesis would have not been possible without the mathematical guidance of Dimitrios Sounas. I want to thank him for helping me through his truly impressive mathematical insight.

Moreover, I want to thank May Choueib for giving me a crash-formation on microfabrication. Without the extensive help she provided me to learn all the techniques and instruments, the experimental side of this work would have taken a great amount of time.

Also, I would like to thank all of the group's members who were always ready to help in any question I threw at them. Special thanks to Hadi and Simon for making office time highly enjoyable.

Finally, I would like to thank my brothers, Joseph and Jihad, and my parents, Najah and Camille, whom without their financial boosts I would not have made it where I am today.

RÉSUMÉ

La génération et l'amplification des ondes hyperfréquences (RF) est au coeur des télécommunications, des satellites artificiels, et de l'optoélectronique. L'industrie électronique cherche constamment à concevoir des amplificateurs plus petits, plus efficaces, et fonctionnant à des fréquences plus élevées. Les nano-matériaux possédant des propriétés uniques peuvent permettre d'obtenir ces caracteristiques dans des amplificateurs qui comblent l'écart entre les tubes à vide et l'état solide. Dans ce mémoire, nous étudions spécifiquement la possibilité d'utiliser des nanotubes de carbone (CNTs) pour l'amplification des ondes RF. En utilisant des moyens théoriques, nous montrons que l'amplification est en effet une possibilité. Également, nous concevons et fabriquons l'appareil de caractérisation nécessaire afin de mesurer et tester la théorie.

Au cours des deux dernières décennies, les CNTs ont prouvé qu'ils possèdent de remarquables propriétés électriques. Deux de ces propriétés motive la pr'esente étude. Premièrement, les CNTs possèdent une grande vitesse de dérive à cause de leur long libre parcours moyen à température ambiante. Par ailleurs, les ondes électromagnétiques de surface le long d'un CNT possède une vitesse de phase grandement ralentie en raison du petit rayon et de l'épaisseur infinitésimale du mur du CNT. Les vitesses de dérive et de phase ont été calculées d'être du même ordre de grandeur, ce qui a grandement motivé cette étude : une telle synchronisation entre le faisceau d'électrons et le champ RF est exactement le mécanisme physique utilisé dans les tubes à ondes progressives (TWT) pour induire l'amplification.

En général, le problème théorique est de calculer le résultat de l'application simultanée des champs RF et continus (DC) sur un métal-CNT. À cette fin, la densité de courant dans une telle situation est d'abord calculée par un problème de transport semi-classique. Ensuite, à travers un couplage avec le problème électromagnétique, une solution de mode propre est atteinte. Enfin, une amplification du champs RF est trouvée au dessus d'un certain seuil pour le champ DC.

En particulier, du point de vue du transport de particules, nous utilisons l'équation de transport de Boltzmann (BTE) pour calculer la répartition des porteurs de charge sous les champs DC et AC. Ensuite, la densité de courant de Boltzmann est calculée en fonction du champ DC. Une conductivité différentielle négative (NDC) est trouvée sous champs DC modérés. En approximant la fonction de dispersion électronique par une fonction linéaire, nous trouvons des solutions analytiques pour la distribution et la densité de courant. Les solutions analytiques et numériques du BTE sont en bon accord.

Du point de vue des ondes électromagnétiques, nous utilisons les équations de Maxwell

pour trouver la solution de la propagation des ondes de surface tout au long d'un conducteur creux tel que le CNT. En utilisant les conditions aux bords à la surface du CNT, nous arrivons à une relation pour la densité de courant. En imposant l'égalité entre les courants calculés en utilisant les points de vue transport et électromagnétique, nous trouvons une équation déterminante dont la solution est la dispersion électromagnétique en fonction du champ DC.

En l'absence d'un champ DC, la lenteur de la vitesse de phase des ondes progressives est attribuée en grande partie à la géométrie du problème. Par contre, la propagation RF est largement modulée avec l'application et l'augmentation du champ DC.

En supposant une dispersion spatiale négligeable, une amplification des ondes RF a été trouvée au-delà d'un seuil de 3×10^5 V/m, signalée par un facteur d'atténuation positif. À ces amplitudes, l'amplification est expliquée dans notre modèle par de réflexions de type Bloch aux bords de la zone de Brillouin (BZ).

Cependant, des calculs préliminaires qui incluent la dispersion spatiale ont aboutis à l'apparition d'un mode amplifié à un champ de 10^4 V/m. En plus, les vitesses de phase et de dérive sont egales à ce champ là, ce qui suggère la possibiltée d'une amplification de type TWT. Malgré que ces derniers resultats sont bruts, ils soulignent l'importance des effets non locaux, qui sont dignes d'un calcul plus rigoureux en utilisant des techniques d'analyse complexe.

Dû à des difficultées techniques, le but du côté expérimental était limité à la conception et la fabrication de l'appareil de caractérisation RF qui pourrait ultérieurement être utilisé pour étudier le problème expérimentalement. Le guide d'onde coplanaire (CPW) a été le guide d'ondes planes de choix grâce à sa polyvalence et capacités haute fréquence. La trace du signal CPW est fuselée et une ouverture permet aux CNTs, idéalement un seul, d'être aligné pour les mesures. Les CNTs ont été déposés sur les substrats en utilisant la methode d'enduction centrifuge comme première étape. Puis, en utilisant le microscope à force atomique (AFM), le dépôt a été raffiné jusqu'à l'obtention de la concentration et de l'alignement souhaités. Ensuite, les électrodes ont été modelés par une lithographie optique suivie par un décollage. Après cette dernière étape, l'alignement à travers les CPWs a été examiné à l'aide du microscope électronique à balayage (SEM). Comme resultats, nous avons trouvé de nombreux CPWs contacté par un ou plusieurs CNTs.

ABSTRACT

Radio-frequency (RF) generation and amplification is at the heart of telecommunication, satellite and optoelectronics applications. The electronics industry is in constant search for RF amplifiers that are smaller, more efficient, and operating at higher frequencies. Nanomaterials with unique properties promise to fulfill these characteristics while bridging the gap between vacuum-based and solid-state amplifiers. In this thesis, we specifically investigate the capability of carbon nanotubes (CNTs) in amplification of traveling-waves at RF frequencies. Using theoretical means, we show that such amplification is indeed a possibility. We also design and fabricate the characterization fixture needed for measurements and testing the theory.

Over the last two decades, CNTs have proved that they possess remarkable electrical properties. Two of these properties incite the following study. First, CNTs possess a large electron drift velocity due to their long mean free path at room temperature. Furthermore, electromagnetic surface-wave propagation along a CNT acquires a large slow-wave factor due to the smallness of the radius and the infinitesimal wall thickness. The drift and phase velocities are calculated to be on the same order of magnitude, thereby immensely motivating this study : such synchronization between the electrons and the RF field is exactly the physical mechanism used in traveling-wave tubes (TWTs) to induce amplification.

In general, the theoretical problem is to investigate the outcome of applying simultaneous DC and RF fields across a metallic-CNT. For this purpose, the CNT current density is first calculated through a semi-classical transport problem. Then, through coupling with the electromagnetic problem, an eigenmode solution is reached. Finally, RF traveling-wave amplification is found above a certain threshold DC field.

Particularly, from the particle's transport perspective, we use the Boltzmann transport equation (BTE) to calculate the distribution of the charge carriers under DC and AC fields. Afterwards, the Boltzmann AC current density is found with respect to the applied DC field. Negative differential conductivity (NDC) is found under moderate fields. By approximating the electronic dispersion of CNTs as a linear function, we find analytical solutions for the distribution and current density that agree reasonably well with the full-band numerical solution of the differential equations.

From the electromagnetic wave perspective, we use Maxwell's equations to find the solution for surface-wave propagation along a hollow conductor which is the CNT. Using the surface boundary conditions, we reach a relation for the Maxwell current density. By equating the currents calculated through the transport and electromagnetic aspects at all points in

space-time, we find a determinantal equation whose solution is the electromagnetic dispersion.

In the absence of a DC field, the immense slow-wave factor in CNTs is attributed largely to the geometry of the problem. On the other hand, the RF propagation is found to be largely modulated by the application and subsequent increase of a DC field.

Assuming negligible spatial dispersion, an amplification was found beyond a threshold value of 3×10^5 V/m, as signalled by a positive attenuation factor. At such fields, the amplification response is explained in our model through Bloch-type reflections at the Brillouin zone (BZ) edges, instead of the expected TWT-like behavior.

However, preliminary calculations that included the spatial dispersion lead to the appearance of an amplified mode at a lower field of 10^4 V/m. Interestingly, the phase and drift velocities are matched at this field magnitude, which suggests a possibility of a TWT-like amplification. However crude, these results point to the importance of the previously neglected non-local effects, which are worthy of a more rigorous calculation that makes use of complex plane analysis techniques.

Due to technical shortcomings, the experimental aim of the work was limited to the design and fabrication of the RF characterization fixture which could later be used to investigate the problem experimentally. The coplanar waveguide (CPW) was the planar waveguide of choice thanks to its versatility and high-frequency capabilities. The CPW signal trace was tapered and a gap opening allowed for CNTs, ideally one, to be aligned for measurements. The CNTs were deposited on the substrates using spin-coating as a first step. Then, using the atomic force microscope (AFM), the deposition was refined to the desired concentration and alignment. Afterwards, the CPW electrodes were patterned using standard optical lithography/lift-off. After this final step, alignment across the CPW gaps was probed using the scanning electron microscope (SEM). As a result, we found numerous CPWs contacted by a single or multiple CNTs.

TABLE OF CONTENTS

DEDICATION iii

ACKNOWLEDGMENTS iv

RÉSUMÉ v

ABSTRACT vii

TABLE OF CONTENTS ix

LIST OF FIGURES xi

LISTE DES ANNEXES xiv

LIST OF ACRONYMS AND ABBREVIATIONS xv

CHAPTER 1 Introduction 1
1.1 Overview and scope of the work 1
1.2 Fundamentals of carbon nanotubes 3
1.2.1 Graphene bandstructure 3
1.2.2 Graphene to carbon nanotube 9
1.3 Literature review : properties and applications of CNTs 14
1.3.1 Electrical properties and devices 14
1.3.2 Other CNT properties and devices 17
1.4 Problem introduction 18
1.4.1 Motivation 18
1.4.2 Objectives 19
1.4.3 Approach 19
1.5 Thesis structure 19

CHAPTER 2 Theoretical Investigation of Amplification 21
2.1 Objectives and justification of approach 21
2.1.1 Objectives 21
2.1.2 Justification of approach 22
2.2 Previous work 23

2.3 Transport problem . . . 24
2.3.1 Electronic energy dispersion . . . 24
2.3.2 Carrier distribution function . . . 25
2.3.3 Surface current density . . . 32
2.4 Electromagnetic problem . . . 39
2.4.1 Surface wave mode (TM_z) for a hollow cylindrical conductor . . . 39
2.5 Electromagnetic dispersion : eigensolution . . . 41
2.5.1 No DC field . . . 41
2.5.2 RF and DC : traveling-wave amplification . . . 42
2.6 Discussion . . . 45
2.6.1 Physical mechanism for amplification . . . 45
2.7 Spatial disperion (non-local effects) . . . 46
2.7.1 Scattering model . . . 47
2.8 Conclusion . . . 49

CHAPTER 3 Fabrication of Characterization Fixture . . . 50
3.1 Introduction . . . 50
3.2 Description of characterization fixture . . . 51
3.2.1 Electromagnetic waveguiding structure . . . 51
3.2.2 CNT contact . . . 53
3.3 Fabrication procedure . . . 54
3.3.1 CNT deposition and alignment . . . 54
3.3.2 Lithography and lift off . . . 55
3.4 Conclusion . . . 59

CHAPTER 4 Conclusion . . . 60
4.1 Summary and contributions . . . 60
4.2 Limitations and future improvements . . . 61

REFERENCES . . . 63

APPENDICES . . . 68

LIST OF FIGURES

Figure 1.1 Graphene is a single atomic sheet of graphite. A CNT is a graphene rolled into an empty cylinder. 4

Figure 1.2 Atomic orbitals of a carbon-carbon bond in a graphene sheet. 5

Figure 1.3 Real space lattice of graphene. Unit cell shown in shade. 5

Figure 1.4 k-space lattice of Graphene. The BZ is shown in shade. 6

Figure 1.5 Energy dispersion diagram of graphene within the BZ. 9

Figure 1.6 Real-space lattice and unit cells of (a) $(3, 0)$ zigzag CNT and (b) $(3, 3)$ armchair CNT. 10

Figure 1.7 k-space lattice and BZ of (a) $(3, 0)$ zigzag CNT and (b) $(3, 3)$ armchair CNT. 11

Figure 1.8 Electronic dispersion diagram of (a) $(3, 0)$ zigzag CNT and (b) $(3, 3)$ armchair CNT. Highlighted region below the Fermi energy corresponds to the valence bands. 13

Figure 2.1 Illustration of traveling-wave amplification along a CNT biased by a longitudinal DC field. 21

Figure 2.2 Energy dispersion of the conduction bands ($\varepsilon > 0$) and valence bands ($\varepsilon < 0$) crossing the Fermi energy level ($\varepsilon = 0$) for an ($n = 3q, 0$) (metallic) zigzag CNT. The solid and dashed curves correspond to the tight-binding and linearized dispersion relations given by (2.1) and (2.2), respectively. 25

Figure 2.3 Reciprocal lattice of graphene showing the equivalence between BZ $\mathrm{BZ}_{\mathrm{Slepyan}}$ for a $(3, 0)$ CNT. The background contour plot is the dispersion relation of graphene while the periodic hexagonal regions are the corresponding 2D BZs. The horizontal bars represent the 1D BZs of the CNT, whose length corresponds to the period of the CNT along the axis (z) of the tube, i.e. u for BZ (double arrowheads) and $2u$ for $\mathrm{BZ}_{\mathrm{Slepyan}}$ (single arrowheads), and whose spacing corresponds to the azimuthal (ϕ) quantization step due to graphene folding into a closed tube, i.e. $p_\phi = p_{\phi,s} = 2\pi\hbar s/(\sqrt{3}na_{cc})$. 26

Figure 2.4 Comparison of the analytical and numerical solutions for the DC distribution function. 33

Figure 2.5 Comparison of the analytical and numerical solutions for the AC distribution function. 34

Figure 2.6 DC Current density of a $(9,0)$ zigzag CNT versus the applied DC electric field, computed numerically by (2.27) via (2.14) and analytically by (2.32). NDC is observed at fields higher than 10^5 V/m. 36
Figure 2.7 AC Conductivity of a $(9,0)$ zigzag CNT versus the DC field at 1 GHz, computed numerically by (2.27) via (2.14) and analytically using (2.33). (a) Wide view (b) Zoom on the region of absolute negative conductivity. 37
Figure 2.8 AC Conductivity, computed using (2.33), for a (9,0) CNT exposed to different values of DC field versus the frequency. 38
Figure 2.9 Electromagnetic dispersion relation $h(\omega) = \beta(\omega) - j\alpha(\omega)$ (2.41) of a metallic zigzag CNT with respect to frequency, calculated with $E_z^{dc} = 0$. 42
Figure 2.10 Phase velocity $v_p(\omega) = \omega/\beta(\omega)$ of the traveling surface waves along a metallic zigzag CNT with respect to frequency, calculated with $E_z^{dc} = 0$. 43
Figure 2.11 Electromagnetic dispersion relation $h(\omega) = \beta(\omega) - j\alpha(\omega)$ (2.41) of a (9,0) CNT exposed to a DC electric field E_z^{dc}, found by solving (2.40) at 1 GHz. 44
Figure 2.12 Comparison between the drifting velocity of the electrons, v_d, and the phase velocity of the traveling waves, v_p. As it can be seen, there is no match of velocity (ie. synchronization) at fields leading to amplification, $E_z^{dc} = 3 \times 10^5$ V/m. 45
Figure 2.13 Distribution function for two different E_z^{dc}, superimposed with the corresponding group velocity v_z, all with respect to the momentum. The distribution of the electrons at the edges of the BZ is non-zero signaling a Bloch-type oscillation. 46
Figure 2.14 The positive propagation constants $\beta > 0$ of the non-local solutions to (2.40) compared to the local case. Without proper complex plane analysis, it is difficult to distinguish between two respective modes. . . 48
Figure 2.15 The attenuation constant α of the non-local modes (with $\beta > 0$) compared with the local case. Taking spatial dispersion into account leads to an amplification at much lower fields around $E_z^{dc} = 10^4$ V/m. 48
Figure 3.1 Illustration depicting the inherent mismatch between CNTs and the macro-world. 50
Figure 3.2 Regular ungrounded CPW. View from (a) top and (b) end side. 51
Figure 3.3 Illustration showing the electric field lines in the fundamental modes of the CPW : (a) even mode and (b) odd mode. 52
Figure 3.4 Characterization fixture setup showing the GSG probes, the tapered CPW, and the gap where the CNT should be aligned across. 53

Figure 3.5 Illustration showing the three TRL structures : THRU, REFLECT, and LINE, respectively. 54
Figure 3.6 Methods for contacting the CNT : bottom contact or top contact . . . 55
Figure 3.7 AFM results after spin-coating : (a) and (b) were measured on the same substrate at different locations with respect to the center where the CNTs are dropped. Inset in (b) shows the vertical displacement of the AFM tip corresponding to the diameter of the CNT. Width of the figures correspond to 5 μm. 56
Figure 3.8 Lithography results : (a) shows the lithography at the edges and (b) shows the tapering of the signal line and the patterning of the gap. . . 57
Figure 3.9 Some of the SEM pictures highlighting : (a) the alignment, (b) and (c) the connection of individual CNTs across the CPW gaps. 58
Figure A.1 Electromagnetic dispersion relation $h(\omega) = \beta(\omega) - j\alpha(\omega)$ (2.41) of a copper conductor found by solving (A.5). 69
Figure A.2 Phase velocity of the surface-wave modes plotted in fig. A.1 for various radii. A substantial decrease in the phase velocity is found for a radius smaller than 1 μm. 69

LISTE DES ANNEXES

Annexe A Surface Wave Mode (TM_z) for a Full Cylindrical Conductor 68

LIST OF ACRONYMS AND ABBREVIATIONS

RF	Radio-Frequency
CNT	Carbon NanoTube
TWT	Traveling-Wave Tube
m-CNT	metallic-CNT
1-D	One-Dimensional
2-D	Two-Dimensional
MWCNT	Multi-Walled CNT
BZ	Brillouin Zone
NDC	Negative Differential Conductance
BTE	Boltzmann Transport Equation
RTA	Relaxation Time Approximation
CPW	Coplanar Waveguide
TRL	Thru-Reflect-Line
GSG	Ground-Signal-Ground
AFM	Atomic Force Microscope
SEM	Scanning Electron Microscope

CHAPTER 1

Introduction

1.1 Overview and scope of the work

Radio-frequency (RF) generation and amplification is at the heart of telecommunication, satellite and optoelectronics applications. Various devices relying on different physical mechanisms achieve said generation and amplification of RF fields. In general, RF amplifiers can be divided into : solid-state, and vacuum-based.

Vacuum devices, such as traveling-wave tubes (TWTs), were the first of such devices historically. They have been mostly replaced by solid-state devices due to their complex, bulky structures and their short life-times. However, they are still being favored in specific applications where higher frequencies, greater power handling, and larger bandwidths are needed such as satellite communications. On the other hand, solid state devices, such as field effect transistors (FETs) and two-terminal devices (eg. Gunn-diodes, tunnel-diodes) are the most widely used in the industry due to their scalability, integrability and efficiency. However, these devices have strong frequency limitations caused by the transit-time effect in transistors, and the finite relaxation time in Gunn-diodes. Furthermore, with the constant miniaturization, transistors are expected to reach their absolute physical limits very soon.

However, nano-materials with unique properties are increasingly being applied towards innovative devices that promise the replacement of bulky semiconductors. These nano-materials, such as carbon nanotubes (CNTs) and graphene, offer the potential of achieving miniature, low-cost, and large bandwidth RF-to-THz amplifiers. Over the last two decades, CNTs have proved that they possess remarkable electrical properties which could lead to a possible widespread integration in the electronics industry. While semiconducting CNTs have been directly put to use for device conception, their metallic counterpart's contributions have been more restricted to the scientific aspect due to the unique features they were shown to possess.

Here, interest in metallic-CNTs (m-CNTs) as RF amplifiers is fueled mainly through two of its properties. First is the high drift velocity saturation of the electrons, which can reach values on the order of 8×10^5 m.s^{-1} [1]. Second, predicted but yet unobserved, a large slow-wave constant for surface electromagnetic waves was found, with phase velocities around 10^6 m.s^{-1} [2]. This seemingly inherent velocity synchronization between the electrons and phase velocity of the photons is reminiscent of traveling-wave tubes (TWTs) which, by engineering such a velocity matching, achieve traveling-wave amplification of radio frequency

(RF) signals with large bandwidth and power capabilities [3]. In TWTs, the RF phase velocity is physically slowed down by a helix to match that of the electrons, which are launched inside the vacuum tube from an electron gun. On the other hand, CNTs seem to provide a natural slow-wave medium with exceptional electron drifting speeds. Driven by this similarity, we speculate the possibility of traveling-wave amplification in m-CNTs when biased with a DC field.

For this purpose, we theoretically investigate the outcome of superimposing DC and RF fields across a m-CNT. Furthermore, we design and fabricate the characterization fixture needed to test the theoretical results.

This chapter first introduces CNTs and their fundamental electronic structure and physics. Moreover, a broad spectrum of the breakthroughs that unveiled their properties and conceived their applications are highlighted. Afterwards, the motivation, goal, and approach of the following work are pointed out. Finally, the structure of the remainder of the thesis is presented.

1.2 Fundamentals of carbon nanotubes

A carbon nanotube (CNT) is a thin, hollow cylindrical tube made entirely of carbon with a diameter typically on the order of a nanometer [4]. CNTs can grow to lengths in the millimeter range, making them quasi- one-dimensional (1-D) structures for any practical purpose. They were first discovered by Ijima in 1991 [5] and quickly became a subject of interest to scientists due to the unique features of their geometry. Their transversal confinement entails that some of their characteristics are largely dictated by quantum mechanics [4]. Rigorous characterization of CNTs yielded exceptional mechanical and electronic properties which promised the conception of many useful applications and resulted in a quick worldwide exposure of CNTs among scientists and technologists alike.

Theoretically, a CNT is a graphene sheet rolled up into a cylinder, while graphene is a monolayer graphite as is illustrated in Fig. 1.1. Therefore, CNTs share the same lattice structure as graphene. In the following sections, the fundamentals of graphene and the properties leading to its electronic properties are first presented. The electronic properties of CNTs are then inferred from those of graphene. The anisotropy of the lattice results in different types of CNTs described through their *chirality* which ultimately explains the metallic or otherwise semi-conducting nature of the CNT [4].

A multi-walled CNT (MWCNT) is another form of CNTs whereby a number of concentric CNTs with increasing radii are equally spaced. MWCNTs are also suited for traveling-wave investigation but will be left out of the discussion to avoid further complicating the theoretical analysis.

1.2.1 Graphene bandstructure

Graphene is a monolayer of graphite. It has the unique property of being a naturally occurring 2-D material. Unlike the CNT, its structure was theoretically known to material scientists long before its recent discovery in [6]. As shown in Fig. 1.2 which illustrates a carbon-carbon bond in graphene, hybrid sp^2 orbitals form σ-bonds and the remaining p_z orbitals form π-bonds. σ- and π- bonds are defined as follows : the axis of σ bonds intersects with the atomic nuclei thereby forming the in-plane bonds, whereas π bonds form out-of-plane bonds which do not intersect a nuclei. σ-bonds in graphene and CNTs shape the materials' strong mechanical properties as they are responsible for their huge stiffness. On the other hand, electron conduction is mediated and essentially takes place through the π-bonds [4]. We can intuitively understand this fact by noticing in Fig. 1.2 that since there are no nulls in the orbitals of a π-bond, electrons are free to move around the lattice and are said to be delocalized, forming a 'connecting' network which explains the conductance of graphene and

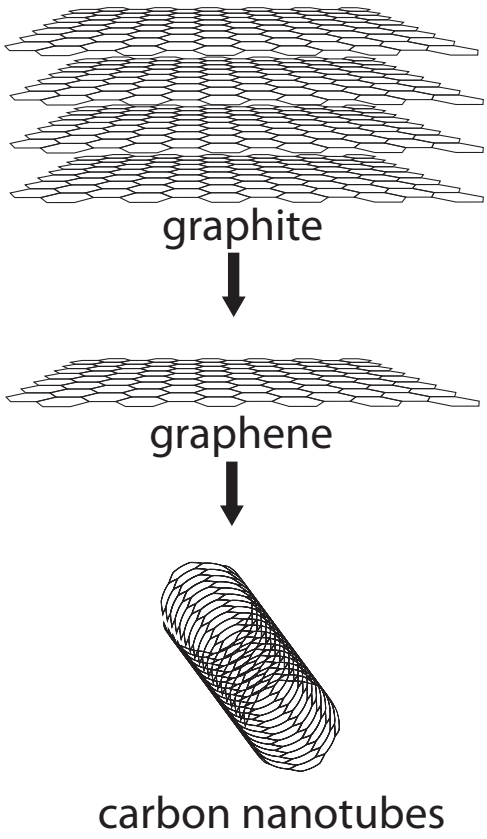

Figure 1.1 Graphene is a single atomic sheet of graphite. A CNT is a graphene rolled into an empty cylinder.

some CNTs.

The 2-D *real-space* lattice is illustrated in Fig. 1.3. The graphene unit cell contains two atoms separated by the interatomic distance $a_{cc} = 1.42$ Å. Its unit vectors may be chosen as

$$\mathbf{a_1} = \left(\sqrt{3}, 1\right)\frac{a}{2}, \quad \mathbf{a_2} = \left(\sqrt{3}, -1\right)\frac{a}{2} \tag{1.1}$$

where $a = |\mathbf{a_1}| = |\mathbf{a_2}| = \sqrt{3}a_{cc}$ is the lattice constant. The unit cell is formed by the two lattice vectors and is highlighted in Fig. 1.3.

On the other hand, the 2-D *k-space* lattice is illustrated in Fig. 1.4. The reciprocal unit vectors, $\mathbf{b_1}$ and $\mathbf{b_2}$, are found from (1.1) through the operation [7]

$$\mathbf{a_i} \cdot \mathbf{b_i} = 2\pi\delta_{ij}, \tag{1.2}$$

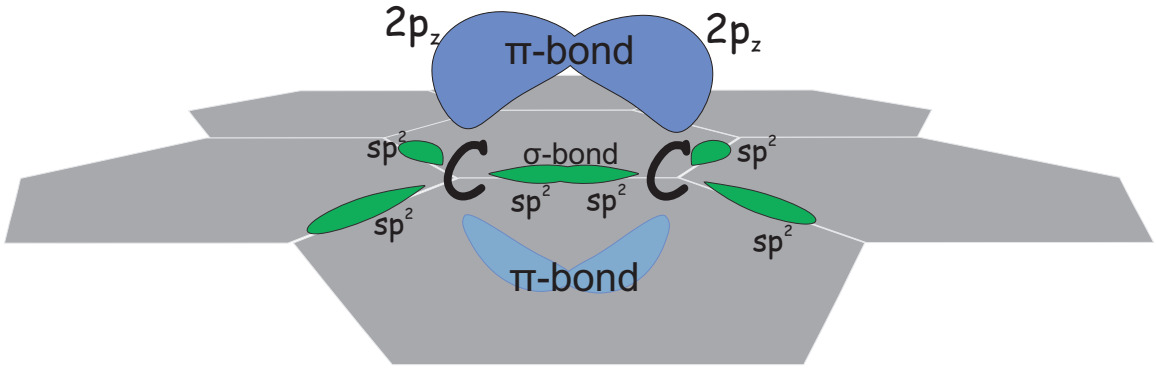

Figure 1.2 Atomic orbitals of a carbon-carbon bond in a graphene sheet.

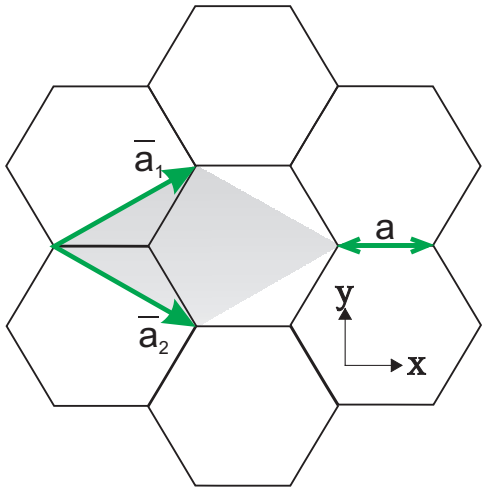

Figure 1.3 Real space lattice of graphene. Unit cell shown in shade.

where δ_{ij} is the Kronecker delta. As a result,

$$\mathbf{b_1} = \left(\frac{1}{\sqrt{3}}, 1\right)\frac{2\pi}{a}, \quad \mathbf{b_2} = \left(\frac{1}{\sqrt{3}}, -1\right)\frac{2\pi}{a}, \tag{1.3}$$

wherefore the reciprocal lattice constant is $b = 4\pi/\left(\sqrt{3}a\right)$. The first Brillouin Zone (BZ) of graphene is highlighted in Fig. 1.4.

The tight-binding model is routinely used to arrive at an analytical form for the electronic energy dispersion or bandstructure, $E(\mathbf{k})$, for graphene. Since solving the Schrödinger equation is practically impossible in such a large system, many approximative models are available with increasing levels of complexity [8]. The tight-binding approximation presents itself as one of the simpler approaches. It assumes tightly bound electrons whose wave-

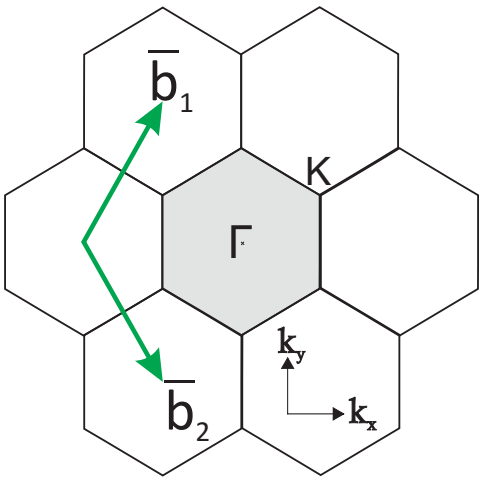

Figure 1.4 k-space lattice of Graphene. The BZ is shown in shade.

functions do not differ greatly from the initial orbital of the individual atoms. This section describes briefly the derivations leading to the electronic dispersion relation of graphene [4]. The main assumptions frequently taken to arrive at the relatively simple analytical solution are as follows :

1. Electron-electron interaction is neglected. ie. It is a one electron model.
2. Only π-bonds contribute to conduction.
3. The nearest-neighbor approximation considers only interactions between neighboring atoms.
4. The graphene structure is infinitely wide, perfectly periodic, and has no defects.

For the purpose at hand, the Schrödinger equation must be solved for an electron subject to the potential of the lattice such as [9]

$$H\Psi_j(\mathbf{k},\mathbf{r}) = \left[-\frac{\hbar^2}{2m}\nabla^2 + U(\mathbf{r})\right]\Psi_j(\mathbf{k},\mathbf{r}) = E_j(\mathbf{k})\Psi_j(\mathbf{k},\mathbf{r}), \tag{1.4}$$

where H is the lattice Hamiltonian, $U(\mathbf{r})$ is lattice potential, m is electron mass, and $E_j(\mathbf{k})$ is the eigenenergy of the eigenfunction $\Psi_j(\mathbf{k},\mathbf{r})$ for the j-th band with wave vector $\mathbf{k}$. Since it is a periodic problem, the eigenfunction (or Bloch function) should satisfy Bloch's theorem [9] giving $\Psi_j(\mathbf{k},\mathbf{r}+\mathbf{R}) = e^{i\mathbf{k}.\mathbf{R}}\Psi_j(\mathbf{k},\mathbf{r})$, where $\mathbf{R} = p_1\mathbf{a_1} + p_2\mathbf{a_2}$ is the Bravais lattice vector with p_1 and p_2 being integers. Therefore the wavefunction is periodic in the reciprocal space with periodicity the reciprocal lattice vector $\mathbf{K} = q_1\mathbf{b_1} + q_2\mathbf{b_2}$, where q_1 and q_2 are integers. In other terms,

$$\Psi_j(\mathbf{k}+\mathbf{K},\mathbf{r}) = \Psi_j(\mathbf{k},\mathbf{r}). \tag{1.5}$$

Therefore, the Bloch function can be written as a Fourier series expansion [9],

$$\Psi_j(\mathbf{k},\mathbf{r}) = \frac{1}{\sqrt{N}} \sum_{\mathbf{R}} e^{i\mathbf{k}.\mathbf{R}} \phi_j(\mathbf{r}-\mathbf{R}), \tag{1.6}$$

where the coefficients $\phi_j(\mathbf{r}-\mathbf{R})$ are the called the Wannier functions and N is the number of unit cells in the lattice. In traditional problems with translational symmetries, the Bloch function basis is chosen to be a plane wave for simplicity. However, for bandstructure calculation problems, a significantly more appropriate choice is that of the atomic orbitals [4]. Moreover, the unit cell contains more than one atomic orbital. Therefore, the Wannier functions which specify the Bloch function in the unit cell can be further approximated by a linear combination of atomic orbitals (LCAO), such that

$$\phi_j(\mathbf{r}) = \sum_{j'=1}^{l} C_{jj'} \psi_{j'}(\mathbf{r}), \tag{1.7}$$

where $\psi_{j'}(\mathbf{r})$ are the atomic orbitals of the two inequivalent atoms within the graphene unit cell, and l is the number of orbitals. As stated, only the π bonds are assumed to contribute to conduction, therefore $l = 2$ corresponding to the $2p_z$ orbitals shown in Fig. 1.2.

Substituting (1.7) into (1.6) and rearranging leads to the expression of the Bloch function as

$$\Psi_j(\mathbf{k},\mathbf{r}) = \sum_{j'=1}^{l} C_{jj'} \Phi_{j'}(\mathbf{k},\mathbf{r}), \quad \text{for} j = 1,2, \tag{1.8}$$

where

$$\Phi_j(\mathbf{k},\mathbf{r}) = \frac{1}{\sqrt{N}} \sum_{\mathbf{R}} e^{i\mathbf{k}.\mathbf{R}} \psi_j(\mathbf{r}-\mathbf{R}), \quad \text{for} j = 1,2. \tag{1.9}$$

Plugging (1.8) into (1.4) gives

$$\sum_{j'=1}^{2} H C_{jj'} \Phi_{j'}(\mathbf{k},\mathbf{r}) = E_j(\mathbf{k},\mathbf{r}) \sum_{j'=1}^{2} C_{jj'} \Phi_{j'}(\mathbf{k},\mathbf{r}). \tag{1.10}$$

Multiplying with $\int \Phi_j^* dr$ on both sides leads to

$$\sum_{j'=1}^{2} H_{jj'} C_{jj'} = E_j(\mathbf{k},\mathbf{r}) \sum_{j'=1}^{2} C_{jj'} S_{jj'}, \tag{1.11}$$

where

$$H_{jj'}(\mathbf{k}) = < \Phi_j | H | \Phi_{j'} >, \qquad S_{jj'}(\mathbf{k}) = < \Phi_j | \Phi_{j'} >, \tag{1.12}$$

are the transfer matrix integral and the overlap integral, respectively. Transforming (1.11) into matrix form gives

$$[\mathbf{H}(\mathbf{k}) - E_j(\mathbf{k})\mathbf{S}(\mathbf{k})]\mathbf{C_j}(\mathbf{k}) = 0 \quad \text{for} \quad j = 1, 2, \tag{1.13}$$

where

$$\mathbf{H}(\mathbf{k}) = [H_{jj'}(\mathbf{k})]_{n\times n} \tag{1.14}$$

and

$$\mathbf{S}(\mathbf{k}) = [S_{jj'}(\mathbf{k})]_{n\times n} \tag{1.15}$$

and

$$\mathbf{C_j}(\mathbf{k}) = [C_{j1}(\mathbf{k})\ C_{j2}(\mathbf{k})]^{\mathbf{T}} \tag{1.16}$$

are the $n \times n$ matrix of the transfer integral, the $n \times n$ matrix of the overlap integral, and $n \times 1$ column eigenvector corresponding to the eigenenergy $E_j(\mathbf{k})$, respectively. Superscript T stands for matrix transpose operation. (1.13) is solved by taking

$$\det[\mathbf{H}(\mathbf{k}) - E_j(\mathbf{k})\mathbf{S}(\mathbf{k})] = 0. \tag{1.17}$$

Evaluating the integrals $H_{jj'}$ and $S_{jj'}$ over the nearest neighbor orbitals, sweeping $\mathbf{k}$ and solving the determinant for the eigenenergies yields the electronic dispersion of graphene. Matrix calculations can be found in [10]. Finally, the graphene bandstructure approximates to

$$E(k_x, k_y) = \pm\gamma_0 \left[1 + 4\cos^2\left(\frac{k_y a}{2}\right) + 4\cos\left(\frac{\sqrt{3}k_x a}{2}\right)\cos\left(\frac{k_y a}{2}\right)\right]^{1/2} \tag{1.18}$$

where γ_0 is the hopping or transfer parameter estimated by first-principles calculations to be around 2.7 eV [11]. As expected, the positive and negative values of the energy refer to the conduction and valence band, respectively. The dispersion is plotted in Fig. (1.5) where it can be seen that graphene has no band gap and is thus a zero bandgap semiconductor or 'semimetal'. However, as is usually the case, the term 'metallic' will be used to describe graphene and CNTs with zero bandgap. The points which cross the Fermi energy are called the K points and they coincide with the hexagon edges. Moreover, much of the properties of low-bias electronic conduction is dictated by the area around the K points [10]. The nearest neighboor approximation provides a good qualitative picture of the electronic dispersion, however, it fails to provide an accurate description which can be provided through density functional calculations [11].

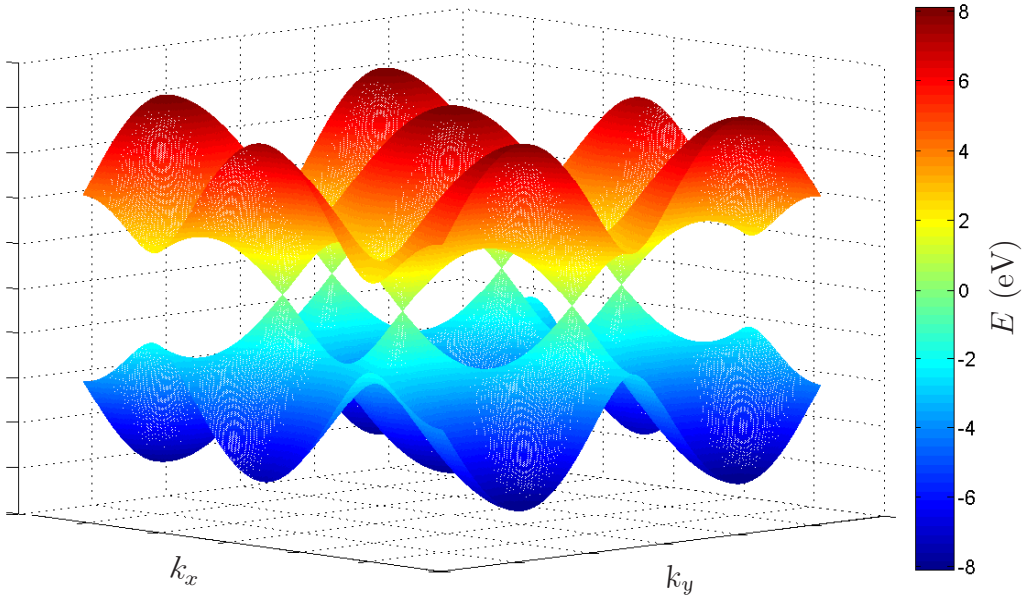

Figure 1.5 Energy dispersion diagram of graphene within the BZ.

1.2.2 Graphene to carbon nanotube

As graphene sheet is theoretically rolled to form a CNT, different angles result in different CNT unit cells and thus in different electronic properties. Analytically, the procedure of arriving to the CNT dispersion from that of graphene is called '*zone folding*', which is an approximative method that works well for larger radius CNTs, but fails as the tube radius is significantly decreased due to the curvature effects. The chiral vector, $\mathbf{C}_h$, describing the angle of folding and the diameter expressed using the unit vectors of the real graphene lattice is shown in Fig. 1.6 and given by [4]

$$\mathbf{C_h} = n\mathbf{a_1} + m\mathbf{a_2}. \tag{1.19}$$

Consequently, the notation (n, m) suffices to specify the CNT under study. Three categories emerge : *armchair* (n, n), *zigzag* $(n, 0)$, and *chiral* (n, m). Furthermore, the magnitude $|\mathbf{C_h}|$ is equal to the circumference of the CNT. On the other hand, the translational vector, $\mathbf{T}$, is the unit vector in the axial direction and is perpendicular to $\mathbf{C_h}$. As can be seen in Fig. 1.6, $\mathbf{T}$ connects the first two identical lattice points in the direction of the axis. It is written as

$$\mathbf{T} = t_1\mathbf{a_1} + t_2\mathbf{a_2}, \tag{1.20}$$

with

$$t_1 = \frac{2m+n}{d_R}, \qquad t_2 = -\frac{2n+m}{d_R}, \tag{1.21}$$

where d_R is the greatest common denominator (gcd) of $(2m+n)$ and $(2n+m)$. The rectangle formed by $\mathbf{C_h}$ and $\mathbf{T}$ is the CNT's unit cell.

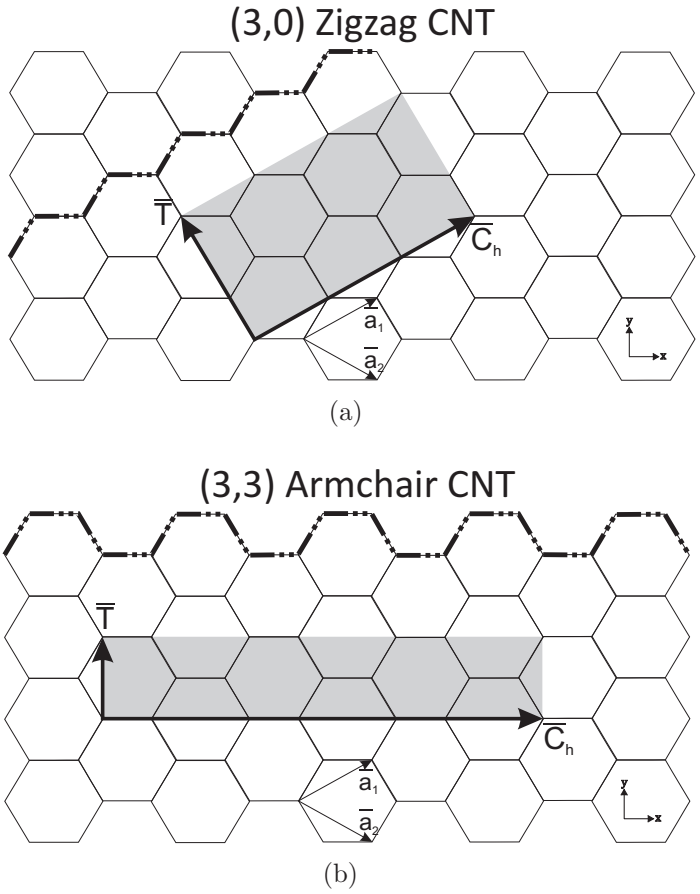

Figure 1.6 Real-space lattice and unit cells of (a) $(3,0)$ zigzag CNT and (b) $(3,3)$ armchair CNT.

The k-space unit vectors, $\mathbf{K_1}$ and $\mathbf{K_2}$, for an (n,m) CNT are found, similarly to (1.2), using the relations

$$\begin{aligned} \mathbf{C}_h \cdot \mathbf{K}_1 &= 2\pi, \qquad \mathbf{T} \cdot \mathbf{K}_1 = 0, \\ \mathbf{C}_h \cdot \mathbf{K}_2 &= 0, \qquad \mathbf{T} \cdot \mathbf{K}_2 = 2\pi. \end{aligned} \tag{1.22}$$

Solving the system of equations (1.22) yields

$$\mathbf{K}_1 = \frac{1}{N}\left(-t_2\mathbf{b}_1 + t_1\mathbf{b}_2\right), \qquad \mathbf{K}_2 = \frac{1}{N}\left(m\mathbf{b}_1 - n\mathbf{b}_2\right), \tag{1.23}$$

where N is the number of hexagons in the real unit cell of CNT. N can also be found as

$$N = \frac{2\left(m^2 + n^2 + mn\right)}{d_R}. \tag{1.24}$$

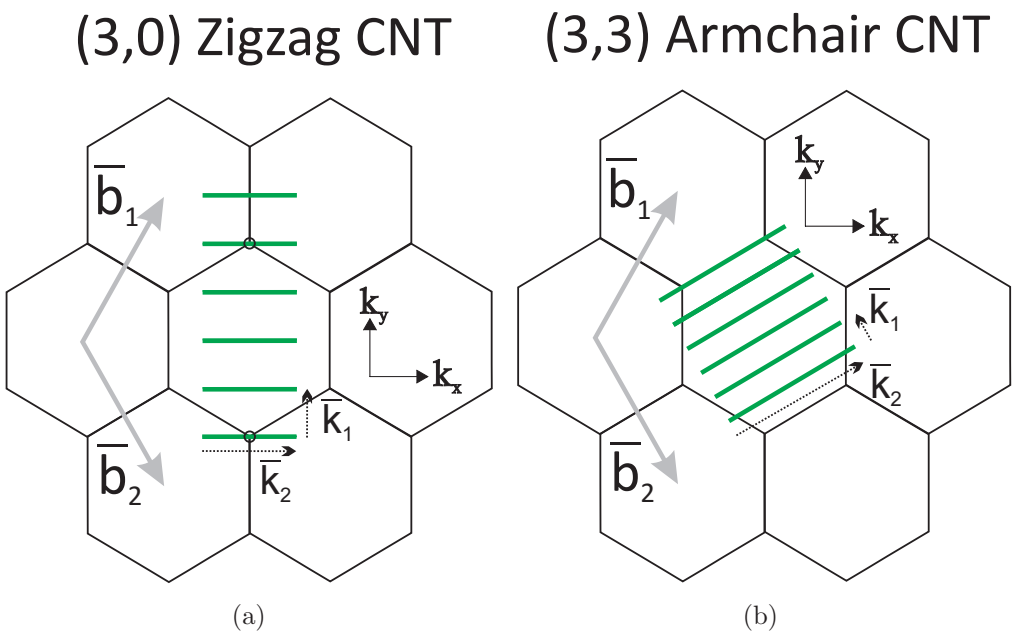

Figure 1.7 k-space lattice and BZ of (a) $(3, 0)$ zigzag CNT and (b) $(3, 3)$ armchair CNT.

Due to the wrapping of the CNT and the consequent cylindrical periodic condition, the wavenumber associated with the azimuthal direction is a multiple of the vector $\mu\mathbf{K_1}$ where μ is an integer. Moreover, it is seen from (1.23) that $N\mathbf{K_1} = (-t_2\mathbf{b}_1 + t_1\mathbf{b}_2)$ and thus only $N\mathbf{K_1}$ corresponds to a graphene reciprocal lattice vector. Subsequently, there exists N quantizations $(\mu = 0, 1, 2, ..., N-1)$ of the azimuthal wavenumber which translate into N sub-bands in the electronic dispersion relation. As a result, the first BZ of a CNT, shown in Fig. 1.7 for zigzag and armchair CNTs, is represented by N parallel lines spaced by $|\mathbf{K_1}|$ and of length $|\mathbf{K_2}|$ each [4].

Shown in the previous section, the K-points which reside at the edges of the graphene BZ coincide with the Fermi points. It follows that, if any of the N lines cross the K-point of the unwrapped hexagonal lattice, the CNT would be of metallic nature, possessing zero band gap. Otherwise, the CNT is semi-conducting. Subsequently, as will be shown, armchair CNTs are metallic, while zigzag and chiral CNTs can be either metallic or semi-conducting. The electronic dispersion relation of CNTs may be easily inferred from that of graphene by considering negligible curvature effects [12], an assumption which is taken throughout the

scope of the thesis. To obtain the dispersion relations, the periodic boundary condition is applied in the circumferential direction

$$|\mathbf{K_1}| \cdot |\mathbf{C_h}| = 2\pi s \tag{1.25}$$

where s is the azimuthal index of the subbands due to quantization.

Zigzag CNTs $(n, 0)$, can be either metallic or semi-conducting. The BZ crosses the K-point, and is therefore metallic, only when $n = 3q$ where q is an integer. Otherwise, it acquires a band gap inversely-proportional to its diameter [13]. For a zigzag CNT, (1.25) translates into

$$k_y na = 2\pi s, \quad \text{for} \quad s = -n + 1, ..., n. \tag{1.26}$$

Substituting k_y from (1.26) into (1.18) and interchanging k_y with k_z as the axial direction yields the 1-D dispersion of zigzag CNTs [4]

$$E(k_z) = \pm t \left[1 + 4\cos\left(\frac{\pi s}{n}\right)\cos\left(\frac{\sqrt{3}ak_z}{2}\right) + 4\cos^2\left(\frac{\pi s}{n}\right) \right]^{1/2}, \qquad \frac{-\pi}{\sqrt{3}a} < k_z < \frac{\pi}{\sqrt{3}a}. \tag{1.27}$$

The dispersion is plotted in 1.8(a) for $(3, 0)$ CNT, of metallic nature, across the first BZ. Two of the sub-bands cross the Fermi energy at the $\Gamma(k_z = 0)$ point. Quick comparison with the BZ diagram in Fig. 1.7(a) verifies that the corresponding sub-bands do cross the hexagone edges at the point specified.

Armchair CNTs (n, n) are metallic because their 1-D BZ always crosses the K-points. Using (1.25) gives the boundary condition that defines the allowed circumferential wave vectors,

$$\sqrt{3}nk_x a = 2\pi s, \quad \text{for} \quad s = -n + 1, ..., n. \tag{1.28}$$

Substituting k_x from (1.28) into (1.18) and interchanging k_y with k_z results in the dispersion of armchair CNTs as [4]

$$E(k_z) = \pm t \left[1 + 4\cos\left(\frac{\pi s}{n}\right)\cos\left(\frac{ak_z}{2}\right) + 4\cos^2\left(\frac{ak_z}{2}\right) \right]^{1/2}, \qquad \frac{-\pi}{a} < k_z < \frac{\pi}{a} \tag{1.29}$$

where k_z is in the direction of $\mathbf{K}_2$ and has the periodicity of $|\mathbf{K}_2|$. Similarly, the dispersion is plotted in 1.8(b).

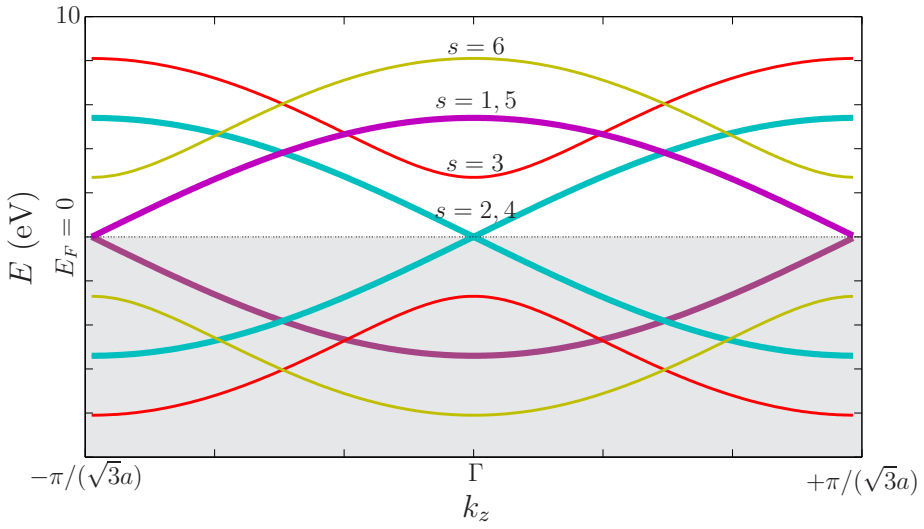

(a)

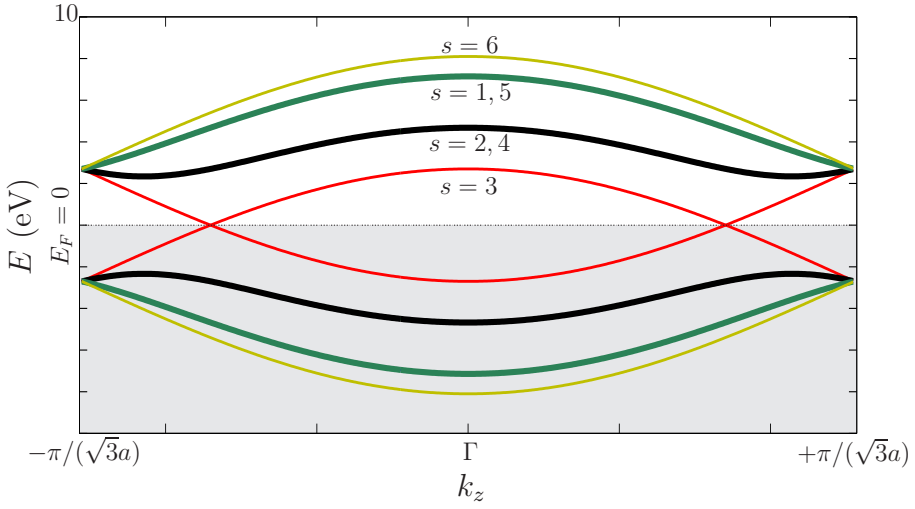

(b)

Figure 1.8 Electronic dispersion diagram of (a) $(3, 0)$ zigzag CNT and (b) $(3, 3)$ armchair CNT. Highlighted region below the Fermi energy corresponds to the valence bands.

1.3 Literature review : properties and applications of CNTs

Despite CNT's relatively simple atomic structure, it offers many intriguing properties [14]. A staggering amount of researchers were drawn to investigate these 1-D structures because of their potential to be integrated in upcoming technologies. Many of these properties can be traced back to the electronic configuration of CNTs : stiff σ-bonds provide the unique mechanical properties, while the π-bonds shape their electrical properties. Some of the most important properties and applications will be listed in this section, with an emphasis on the electrical aspects which are most relevant to the pertaining thesis.

1.3.1 Electrical properties and devices

The fact that CNTs could take either metallic or semiconducting forms fueled the initial interest in studying this unique material. Further investigation lead to the unveiling of numerous different and sometimes unique properties. Due to this, CNTs are especially attractive for computing applications, where they promise to contribute in solving many problems that are arising in the microelectronics industry due to the constant miniaturization (Moore's law). For example, interconnect failure due to electromigration in copper at high current densities triggers an urgency to find a replacement for copper. Furthermore, semiconducting silicon devices are also approaching a fundamental limit with respect to their down-scaling. This section will present the paramount advances that have made CNTs strong candidates for future nanoelectronics. More weight will be given to metallic CNTs in this subsection which is divided into the static and dynamic response.

1.3.1.1 CNTs under static electric fields

Electronic conduction in CNTs is described by its bandstructure, especially around Fermi energy E_f. While the $E-k$ diagram of semiconducting CNTs is fairly similar to regular semiconductors, metal CNTs possess a unique dispersion that is only shared by graphene. Knowing that the group velocity v_g of the electron wave in a certain subband is equal to the slope of the $E-k$ curve [9], and after fast inspection of Fig. 1.8, fast electron dynamics are readily expected around the Fermi point in metallic CNTs.

Metallic CNTs have attracted condensed matter physicists who were able to probe many solid-state theories and concepts in this unique 1-D system of free electrons. At low fields, the electron mean free path was empirically calculated to be in the micron range at room temperature [15]. Therefore, CNTs shorter than the mean free path exhibit ballistic conduction where its conductance is nearly equal to the maximum quantum of conductance $4e^2/h$

[16], proving that little to no scattering occurs in good quality CNTs at low-bias. The main reasons for this phenomenon lie in the ordered crystalline nature of the CNTs, and the long range mean free path for the acoustic phonons. However, as the bias increases, scattering increases thereby decreasing the conductance. Optical phonon emission was shown to be the mechanism behind the increased scattering [17].

Monte Carlo simulations yielded drift velocity saturation velocities to same order of the Fermi velocity ($v_F \approx 8\times10^5$ m/s) [18]. Furthermore, negative differential conductance (NDC), whereby current decreases with an increase of the electric field, has been theorized to exist in CNTs [19; 18]. However, it has only been shown to exist in CNTs suspended over a trench [20]. Albeit yet unsettled, discussions around the origins of the NDC in suspended CNTs point towards the possibility of out-of-equilibrium optical phonons that result in increased electron scattering with a further increase in the applied field [20]. Another feasible physical mechanism is that of electrons jumping to subbands with larger effective mass [18]. The importance and potential use of NDC in CNTs shall be emphasized at later stages.

Semiconducting CNTs , on the other hand, were quickly put to device implementation as their device properties and response do not differ immensely from regular semiconductors. Besides acquiring a band gap inversely proportional to its diameter [13], the ballistic nature of short CNTs yields electron mobilities $\mu > 100,000$ cm^2/(Vs) at room temperature [21]. All of this resulted in the conception and demonstration of cutting-edge electronic devices such as rectifiers [22] and FETs [23]. Ambipolarity, in which the electrons and holes conduct equally well, was also found in CNTs [24].

1.3.1.2 CNTs under dynamic electric fields

The high-frequency properties of CNTs are increasingly being investigated, however the amount of literature on this topic remains far less than that of CNTs exposed to a DC field. The theoretical efforts in revealing the potential of CNTs in serving as nano-waveguides, nano-antennas, and high-frequency FETs will be reported in this section. However, and in contrast to DC electron transport, measurements of the RF response present significant difficulties that experimentalists are yet to overcome in order to achieve any practical RF devices.

Modeling the RF response of CNTs yielded interesting predictions. Both simplistic circuit models and rigorous solutions to the Boltzmann equation have been studied in the literature.

The transmission line model is a simple and effective way to describe passive high-frequency behavior in CNTs. As with all nanostructures, CNTs possess a finite number

of electron states brought forth by the spatial confinement. This results in a *quantum capacitance* which quantifies the energy it takes to add a charge above the Fermi energy. The quantum capacitance, C_Q, is given by [25; 26]

$$C_Q = \frac{4e^2}{\pi\hbar v_F}. \tag{1.30}$$

On the other hand, due to the speeding electrons, CNTs acquire an excess kinetic energy. Unlike the usual magnetic inductance, the kinetic inductance, L_K, has no effect on adjacent CNTs. It is calculated as [25]

$$L_K = \frac{\pi\hbar}{4e^2 v_F}. \tag{1.31}$$

Subsequently, an RF transmission line model can be extracted by adding the quantum circuit elements (C_Q,L_K) with their corresponding classical circuit elements (C_e,L_m), namely, the electrostatic capacitance and the magnetic inductance, respectively. For a CNT above a conducting ground, the RF transmission line model was presented by Burke [26] and it was shown that the wave travels at nearly Fermi velocity v_F. This model, however, is only valid at low-bias because it assumes ballistic transport.

More rigorously, Slepyan et al. previously used the Boltzmann transport equation (BTE) to find an analytical form for the surface conductivity of CNTs [2]. Furthermore, by coupling the BTE solution with that of Maxwell's for a surface electromagnetic wave along a hollow cylinder, the electromagnetic dispersion relation was found. This critical study revealed a slow-wave propagation along the tube, 2 to 3 orders of magnitude slower than the speed of light at RF frequencies. A finding which in turn explains the large kinetic inductance.

Later, Hanson [27] theoretically investigated the transmitting properties of CNTs by solving conventional antenna equations using the surface conductivity found in [2]. Results revealed that CNTs used as dipoles would resonate at much lower frequencies than classical dipoles due to the slowed down nature of the surface waves (ie. surface plasmons). For example, a CNT in the micron range would begin to resonate at a frequency around 1 THz, which is almost 2 orders of magnitude less than a conventional dipole's resonant frequency.

Measuring the RF response faces many intricate challenges that hinder the possibility of a direct characterization of an individual CNT. Instead, the collective excitation and characterization of the effective properties provided an easier approach. An experiment that investigated the radiation properties for an array of CNTs found antenna-like properties which fueled speculations about the potential of CNTs as nano-antennas [28]. On the other hand, a handful of transmission measurements were performed using planar waveguide structures such as Coplanar Waveguides (CPW) to excite CNTs aligned across a gap [29; 30; 31]. Most

notable was the direct measurement of the kinetic inductance of a single CNT by the group at Intel [31].

However, a great difficulty faced by all of the CNT-based high-frequency devices is the high characteristic impedance of CNTs which results in a large reflection coefficient. In other terms, due to the inherent mismatch between macroscopic structures and CNTs, most of the energy impinging at the interface is reflected. Therefore, accurate calibration and de-embedding techniques must be utilized in order to characterize the CNTs, such as the Thru-Reflect-Line (TRL) technique which will be introduced in Chapter 3. One solution to overcome this issue, albeit technologically difficult, is to align the CNTs in arrays to reduce the impedance.

1.3.2 Other CNT properties and devices

1.3.2.1 Mechanical and electromechanical

The mechanical properties of CNTs are closely related to those of graphene because they share the same atomic structure. In such nano-structures with vanishing wall thickness, it is difficult to estimate the Young modulus theoretically. The current convention for the thickness is 0.34 nm, which is the seperation distance of between consecutive graphene sheets in graphite. Such a value for the thickness yielded estimations of the Young modulus to be around 1 TPa [32]. Experimental verification came through two different approaches, namely that of electromechanical resonance [33] and AFM-characterization[34]. Almost equal to the Young modulus of diamond, this value places CNTs among of the world's stiffest materials. Another property CNTs were found to possess is that of interlayer sliding in MWCNTs. Weak Van Der Waals forces were found to ease the sliding and rotational movement of relative nanotubes [35].

The combined stiffness and maneuverability meant that CNTs were appropriate candidates for nanoelectromechanical systems (NEMS) and many interesting applications have seen been published [32]. Among those, the first nano actuator [36], nano-switches [37], a low-friction bearing [38], and an electromechanical resonator that was used as a mass detector with resolution down to 10^{-18} g [39].

1.3.2.2 Field emission

Large aspect ratio, mechanical strength, temperature stability, small response time, low power, and chemical inertness make individual CNTs the near-perfect electron emitters. Therefore, many devices emerged such as field emission displays and x-ray sources. However, the need of large areas with stable, uniform emission has slowed down what otherwise would have seen CNTs take over every field emission device [14].

1.4 Problem introduction

1.4.1 Motivation

Despite the technological difficulties that delayed the exploitation of the properties CNTs offer, theoretical investigations could still look out for possibilities while anticipating the inevitable resolutions brought forth by the experimentalists.

Equipped with such perspective, the investigation of using CNTs as nano-scale amplifiers is not a far fetched concept. Thanks to their mechanical strength and flexibility, infinitesimal width, chemical inertness and great heat capacity, CNTs may prove to be the building blocks for future amplifiers. Here, we highlight the possibility that may have been glossed over in CNTs and how it motivates the present work.

1.4.1.1 Fast electrons, slow waves : analogy with TWTs

As mentioned in the previous section, the drifting velocity of electrons in a CNT can, in theory, reach values as high as 8×10^5 m/s. On the other hand, the phase velocity of RF signals propagating along CNTs slows down to the same order [2]. Despite these values being calculated independently, speculations regarding the possibility of synchronization and interaction between the DC and AC energies is by itself a motif for further investigation [40].

Particular similarity can be drawn with traveling-wave tubes (TWTs) which specifically seek and use this velocity synchronization to induce the coupling of the corresponding DC and AC fields, and a consequent exchange of energy from DC to AC. Generation and amplification of the RF signal in TWTs has been particularly successful as they are still being preferred over the solid state amplifiers in some applications [3].

At first glance CNTs seem to be the perfect nano- counterpart of TWTs for several reasons :

- Slow-wave structure : TWTs use a helix to slow down the wave in one direction, while CNTs achieve this naturally due to its infinitesimal thickness and diameter, as will be shown later.
- Fast electrons : TWTs accelerate and launch a beam of electrons in vacuum, while in m-CNTs electrons barely scatter and consequently possess a large drift velocity.
- Synchronization of the electron-wave velocities : CNTs seem to possess the inherent match which TWTs require careful design to achieve.
- Electron beam confinement : electrons are confined to the surface of the CNT while in a TWT, a bulk magnet achieves the confinement of the beam in vacuum.

Further motivation can be found in the advantages that traveling-wave amplification can offer, namely a large bandwidth and high power capabilities.

Therefore, it can be concluded that such a problem is one worth investigating, despite the difficulties in modeling and the limited technological advancement.

1.4.2 Objectives

Divided into *theoretical* and *experimental*, the ultimate objectives of this work are :

1. Using theoretical means, investigate traveling-wave amplification of RF fields in DC biased m-CNTs.
2. Design and fabricate a characterization fixture that can be used to perform the subtle high-frequency experiments to test the theory.

1.4.3 Approach

The approach used for each of the objectives stated are :

1. – From the transport aspect, we use the Boltzmann transport equation (BTE) in order to find the AC current density, J^{ac}_{BTE}, of a m-CNT subject to both AC and DC fields.
   – From the electromagnetic aspect, we use Maxwell's equations to find a relation for the AC current density, J^{ac}_{BTE}, of the proper mode propagating along a hollow conducting tube which is the CNT.
   – Finally, we couple the particle and wave equations by equating the current densities ($J^{ac}_{\mathrm{BTE}} = J^{ac}_{\mathrm{Maxwell}}$) and solve the eigen problem to find the dispersion relation of the surface electromagnetic waves.
   – Using the electromagnetic dispersion, we find the amplification of the traveling-wave while sweeping the DC field.
2. – Design and simulate a planar electromagnetic structure, in this case a coplanar waveguide (CPW), which will be used to excite and measure the response of individual or otherwise array of parallel CNTs aligned across a short gap.
   – Use self-assembly to disperse and align the CNTs along a certain direction on a substrate.
   – Perform optical lithography- metal evaporation - lift off to pattern a number of CPW structures on the substrate in the direction of the underlying CNTs.
   – Using the scanning electron microscope (SEM), probe the potential alignment and positioning of a single or multiple CNTs across the CPW gap.

1.5 Thesis structure

Pertaining to the objectives enumerated above, the thesis will be structured as follows :

– Chapter 2 takes on the theoretical aspect by sequentially solving the transport problem (BTE), the electromagnetic problem (Maxwell's equations), and the combined eigen problem. Then the solution of amplification, it's physical origins and the possibility of achieving it experimentally will be discussed.
– Chapter 3 presents the CPW as the waveguide structure of choice, and describes the efforts leading the alignment of the CNTs across CPW electrodes. Generally, we present the fundamental issues needed to reproduce the structure.
– Chapter 4 concludes on the results of the theoretical and experimental aspects, offers a discussion on the implications of the present thesis and suggests the tentative next steps as a continuation of this thesis.

CHAPTER 2

Theoretical Investigation of Amplification

2.1 Objectives and justification of approach

2.1.1 Objectives

The goal of this chapter is to theoretically investigate the possible traveling-wave amplification in a m-CNT subject to both AC and DC fields as illustrated in Fig. 2.1. In other terms, this chapter eventually seeks to answer the question : could a m-CNT biased by a DC field provide amplification to a propagating AC signal ?

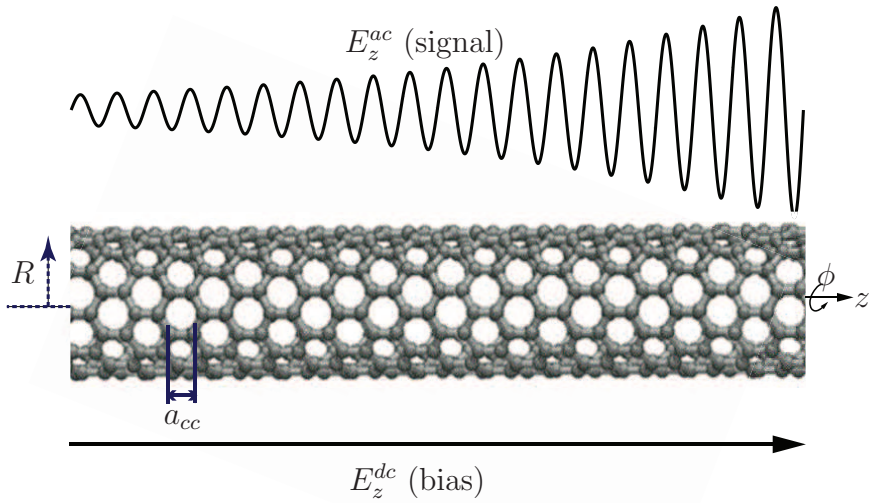

Figure 2.1 Illustration of traveling-wave amplification along a CNT biased by a longitudinal DC field.

For this purpose, we model the response of superimposing an AC field (typically an RF signal) with a DC field along a m-CNT. The sought-after result provides the propagation characteristics which qualify and quantify the traveling-wave's amplification or attenuation by the applied DC field.

2.1.2 Justification of approach

The general approach taken to solve the problem is divided into two aspects : transport and electromagnetic. Whereby from the transport aspect, the BTE is used to calculate the current density, J^{ac}_{BTE}, while an electromagnetic analysis will make use of Maxwell's equations and boundary conditions to find a relation for the current density, here $J^{ac}_{\mathrm{Maxwell}}$. The two currents will be forced to equality at all points in space and time, which will form a determinantal equation whose solution is the electromagnetic dispersion relation $h(\omega)$ where $h = \beta - j\alpha$ is the complex propagation factor. Thereupon, the sought after result lies in the attenuation coefficient α.

Why BTE ? Due to the transversal confinement of the electrons, and the nature of the infinitely thin walls of a CNT, the transport properties are essentially dictated by quantum mechanics and classical dynamics formulations fail to describe the problem correctly. Therefore, an accurate description of the problem may be found using first-principles. However, embarking on such an approach would prove hard to solve and require immense numerical efforts.

On the other hand, semiclassical dynamics are sufficient to capture the essence of the problem at hand. The electrons will be considered as classical particles, moving through a potential with a quantum mechanically calculated bandstructure $E(k)$, where the electron distribution f and thereby the current J are calculated through a stochastic technique, ie. the BTE. We justify the use of the BTE with the following [41] :

- The CNT is long enough so that the position of the electron along the axis of the tube (z direction) is relaxed. Therefore, the uncertainty principle entails that the electron momentum and energy are sharply defined. Consequently, the electron wavepacket may be considered as a classical particle with a definite energy.
- Electron concentration is sufficiently dilute so that the electron-electron correlation is appropriately neglected by BTE.
- The applied potential is sufficiently weak so that tunneling and reflection can be neglected and thus the bandstructure $E(k)$ calculated in the absence of a bias remains valid. Instead, the potential at each position will be assumed to be a superposition of the tight-binding bandstructure and the applied potential $E(k, z) = E(k) + E_z(r)$, where E_z is the total applied field.

Therefore, for the purpose of the analysis of this problem, the BTE will be used to describe carrier transport. Loose approximations have been made in order to justify its use. However, stricter assumptions will have to be done as to the scattering events in order to solve the equation, as shall be explained later.

2.2 Previous work

Cited earlier, the theoretical work of the Belarus group [19; 2; 40] has significantly influenced our thesis and approach.

First, they put forward the problem of applying simultaneous AC and DC excitations across a CNT [40]. Solving the BTE in the time domain, they observed instabilities of AC field at certain bias values and speculated on the possible amplification it could lead to under the right conditions. However, their calculations were based on a helical lattice model, whose electronic dispersion deviates from that of the real CNT hexagonal lattice structure. Furthermore, their transport calculations, done through the BTE, were not coupled with electromagnetic theory to yield a strict solution pointing to amplification.

Later on, the group used the dispersion found through the tight-binding model to calculate an analytical solution for the spatially non-dispersive AC conductivity of both zigzag and armchair CNTs [2]. Then, using the combined BTE-Maxwell approach, the dispersion relation of the surface electromagnetic waves along a CNT was found. This work also quantified the immense slow-wave propagation along a CNT, $2-3$ orders of magnitude below the speed of light.

Afterwards, the DC transport problem was aimed at with relatively high-fields in [19]. NDC characteristics in the $I-V$ curve were found for both metallic and semiconducting CNTs, giving promise for Gunn-type devices[42]. However, the underlying physical mechanism for this prediction was not described.

2.3 Transport problem

2.3.1 Electronic energy dispersion

As presented in 1.2.2, the electronic energy dispersion of CNTs may be deduced by zone-folding the dispersion of graphene, which itself is found through a nearest-neighbor tight-binding calculation involving the delocalized π electrons of carbon atoms [4]. In the following treatment, only metallic zigzag CNTs will be considered. Armchair CNTs can be shown to exhibit approximately the same response as zigzag CNTs, due to their similar band structure around the Fermi point. Neglecting CNT curvature correction [12], the dispersion relation of zigzag $(n, 0)$ CNTs reads [4]

$$\varepsilon(p_z, s) = \pm\gamma_0 \left[1 + 4\cos\left(\frac{\pi s}{n}\right)\cos\left(\frac{3a_{cc}p_z}{2\hbar}\right) + 4\cos^2\left(\frac{\pi s}{n}\right) \right]^{1/2}, \tag{2.1}$$

where, to avoid confusion with the electric field, the energy will be represented by ε from here on. Furthermore, $p_z (= \hbar k_z)$ is the z component of the crystal momentum, which is parallel to the CNT axis. Since the considered CNTs are metallic zigzag tubes, we have $n = 3q$, where q is an integer [4]. The one-dimensional dispersion curves of the bands contributing the most to the current in a metallic zigzag CNT, which are the bands passing through the Fermi energy level, i.e. with $s = \pm q$ and $s = \pm 2q$, are plotted in Fig. 2.2. Taking the Taylor approximation of the cosine function of the momentum near the Fermi points, setting $s/n = \pm 2/3$, noting that $3a_{cc}p_z/(2\hbar) \ll 1$, and considering the Fermi velocity $v_f = 3a_{cc}\gamma_0/(2\hbar)$ [10], (2.1) reduces to the linear approximation

$$\varepsilon(p_z) \approx v_f |p_z|, \tag{2.2}$$

This linear approximation is included in Fig. 2.2 for comparison with the curves calculated through tight-binding. In this study, both the exact (2.1) and the approximate (2.2) dispersion relations are considered.

The Brillouin zone (BZ) of CNTs may be represented by one-dimensional segments when superimposed over graphene's two-dimensional reciprocal lattice, as was shown in sec. 1.2.2. Fig. 2.3 illustrates the BZ for a $(3, 0)$ CNT [4]. The BZ range, defined in sec. 1.2.2 can be written as $-u/2 < p_z < u/2$, where $u = 2\pi\hbar/(3a_{cc})$, with $s = -n + 1, \ldots, n$ [4], which corresponds to the spectral period of the dispersion relation with the subbands considered *collectively*. Slepyan *et al.* alternatively defines $\mathrm{BZ}_{Slepyan}$ as the range $-u < p_z < u$, with $s = 1, \ldots, n$ [40], which corresponds to the spectral period of the dispersion relation with the subbands considered *individually*. In BZ, the subbands extend from $s = -n + 1$ to $s = n$,

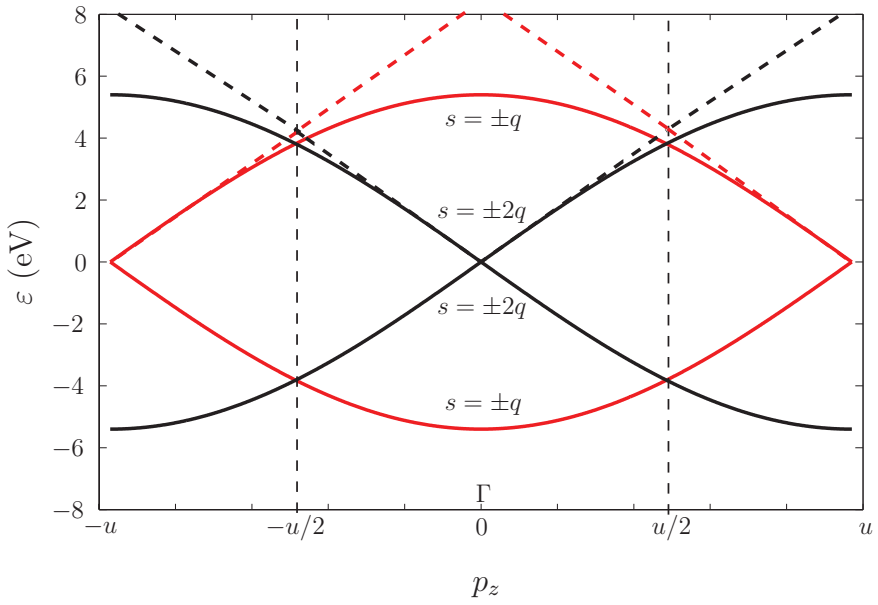

Figure 2.2 Energy dispersion of the conduction bands ($\varepsilon > 0$) and valence bands ($\varepsilon < 0$) crossing the Fermi energy level ($\varepsilon = 0$) for an $(n = 3q, 0)$ (metallic) zigzag CNT. The solid and dashed curves correspond to the tight-binding and linearized dispersion relations given by (2.1) and (2.2), respectively.

while in $\mathrm{BZ}_{Slepyan}$ they extend from $s = 1$ to $s = n$. These two choices are equivalent due to the periodicity of the graphene lattice, as may be seen in Fig. 2.3. For instance, segments e_1 and e_2 of subband $s = -2q$ are equivalent to segments g_1 and g_2 of subband $s = q$, respectively, and therefore extend BZ's subband $s = q$ to the single arrowhead bar shown at $s = q$, which is $\mathrm{BZ}_{Slepyan}$. In other words, $\mathrm{BZ}_{Slepyan}$'s double-length bar at $s = q$ accounts for *both* BZ's bars at $s = -2q$ and $s = q$. Similarly, BZ's subband $s = -q$ and $s = 0$ are merged to $\mathrm{BZ}_{Slepyan}$'s $s = 2q$ and $s = 3q$ bands.

2.3.2 Carrier distribution function

In order to find the current density along the DC-biased CNT, we must find the carrier distribution function $f(z, p_z, t)$ which can be seen as a probability distribution of the electrons with respect to momentum, space, and time. This distribution may be calculated by solving the BTE, which, in its most general form, writes

$$\frac{df(z, p_z, t)}{dt} = \hat{C} f(z, p_z, t) \tag{2.3}$$

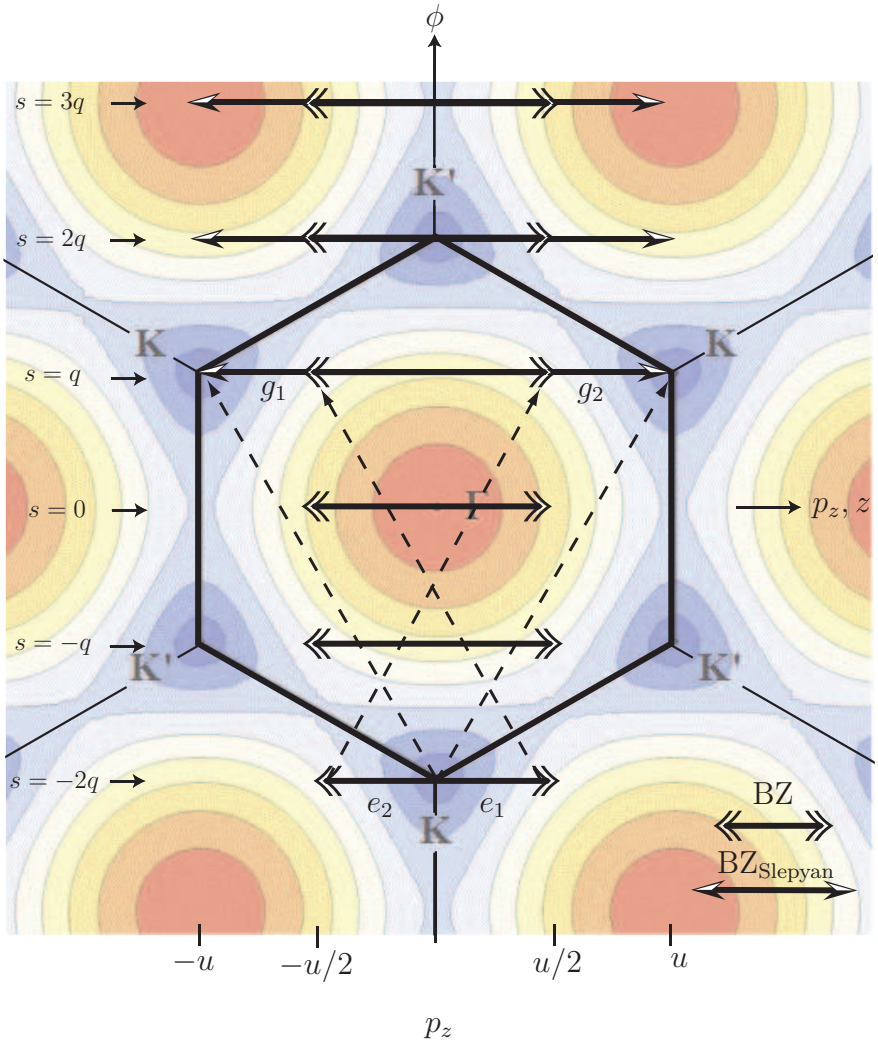

Figure 2.3 Reciprocal lattice of graphene showing the equivalence between BZ $\mathrm{BZ_{Slepyan}}$ for a $(3, 0)$ CNT. The background contour plot is the dispersion relation of graphene while the periodic hexagonal regions are the corresponding 2D BZs. The horizontal bars represent the 1D BZs of the CNT, whose length corresponds to the period of the CNT along the axis (z) of the tube, i.e. u for BZ (double arrowheads) and $2u$ for $\mathrm{BZ_{Slepyan}}$ (single arrowheads), and whose spacing corresponds to the azimuthal (ϕ) quantization step due to graphene folding into a closed tube, i.e. $p_\phi = p_{\phi,s} = 2\pi\hbar s/(\sqrt{3}na_{cc})$.

where $\hat{C}$ is the collision operator which entails the information of all the possible scattering events and is the most difficult term to obtain accurately. A widely-used approximation which provides a greatly-simplified path towards the solution of this equation is the relaxation-time approximation (RTA)[41], a central assumption in our derivation. Under the RTA, and taking the total derivative of the left hand side in (2.3), the BTE takes the form

$$\frac{df(z,p_z,t)}{dt} = \frac{\partial f}{\partial t} + v_z\frac{\partial f}{\partial z} + F_e\frac{\partial f}{\partial p_z} = -\frac{f-F_0}{\tau}, \tag{2.4}$$

where $v_z(p_z) = \partial\varepsilon/\partial p_z$ is the electron group velocity, F_0 is the equilibrium carrier distribution, $\tau = 3\times10^{-12}$ s is the scattering time in CNTs [43], and F_e is the force exerted on electrons by the DC and AC electric fields. This force is given by

$$F_e = -e(E_z^{dc} + E_z^{ac}), \tag{2.5}$$

where E_z^{dc} is the axial (z-directed) DC biasing electric field, assumed constant along the CNT, and E_z^{ac} is the axial AC electric field, assumed to have the time-harmonic traveling waveform

$$E_z^{ac} = \mathrm{Re}[E_{z0}^{ac}e^{j(hz-\omega t)}], \tag{2.6}$$

where E_{z0}^{ac} is the AC field magnitude, h is the complex electromagnetic propagation factor along the CNT and ω is the angular frequency. The equilibrium distribution, $F_0(\cdot)$, is the Fermi-Dirac distribution $F_0(p_z) = 1/[1+e^{\varepsilon(p_z)/(k_BT)}]$, where k_B is the Boltzmann constant and T is the temperature. The BTE (2.4) holds separately for each CNT subband since interband transitions are considered negligible. It is important to note, for later developments, that $f(z,p_z,t)$ is periodic in $p(z)$, with period $2u$, corresponding to Slepyan's BZ choice (Fig. 2.3). This may be shown as follows. Since $\varepsilon(p_z)$ is periodic in p_z (Sec. 2.3.1), so is $F_0(p_z)$, and hence $\tau df/dt + f = F_0$ in (2.4); therefore $f(z,p_z,t)$ is necessarily also periodic in p_z with period $2u$.

The carrier distribution f may be seperated into its DC and AC parts as [44]

$$f = f^{dc} + f^{ac} = f^{dc} + \mathrm{Re}[f_0^{ac}e^{j(hz-\omega t)}]. \tag{2.7}$$

Spatial Dispersion, which can be viewed as space- dependent conductivity, is often assumed to be negligible in the literature [40; 2; 19]. This is done by setting the propagation factor $h(\omega)$ to zero in the BTE, based on the presumption that $\lambda_g >> l_{mfp}$, where λ_g is the guided electromagnetic wavelength and l_{mfp} is the electron mean free path, a characteristic of a local conductivity medium (no spatial dispersion). Furthermore, a vanishing h allows us to arrive at an analytical solution to the problem, which is usually a further motivation for such approximation[2]. Therefore, unless otherwise stated, locality or negligible spatial dispersion will be assumed for the moment. On the other hand, Section 2.7 takes the spatial dispersion into account, re-solves the problem, and discusses the results and the validity of the locality assumption.

As a result, (2.7) becomes

$$f = f^{dc} + f^{ac} = f^{dc} + \mathrm{Re}[f_0^{ac} e^{-j\omega t}]. \tag{2.8}$$

Assuming steady-state regime and spatial uniformity for the DC distribution (by definition of DC), we have $\partial f^{dc}/\partial t = 0$ and $\partial f^{dc}/\partial z = 0$, respectively. Inserting (2.8) and (2.5) into (2.4) with these assumptions yields

$$-j\omega f^{ac} - e(E_z^{dc} + E_z^{ac})\frac{\partial (f^{dc} + f^{ac})}{\partial p_z} = -\frac{f^{dc} + f^{ac} - F_0}{\tau}. \tag{2.9}$$

The DC and AC terms of this relation may be separated from each other to form a relation of the type $\psi_0 = \chi(t)$, where ψ_0 is a time-independent function (formed exclusively by DC terms) and $\chi(t)$ is a time-dependent function (formed by both AC terms and combined AC-DC terms). For this equality to hold *at all times*, we must have $\chi(t) = 0$ and therefore $\psi_0 = 0$. Consequently, within the small-signal approximation, (2.9) splits into the DC and AC equations

$$\psi_0 = \frac{\partial f^{dc}}{\partial p_z} - \frac{1}{\Delta p_z} f^{dc} + \frac{F_0}{\Delta p_z} = 0, \tag{2.10a}$$

$$\frac{\chi(t)}{e^{-j\omega t}} = \frac{\partial f_0^{ac}}{\partial p_z} - \frac{\Omega}{\Delta p_z} f_0^{ac} + R_a \frac{\partial f^{dc}}{\partial p_z} = 0, \tag{2.10b}$$

respectively, where $\Delta p_z = e\tau E_z^{dc}$, $\Omega = 1 - j\tau\omega$ and $R_a = E_{z0}^{ac}/E_z^{dc}$. Equation (2.10a) is known as the 1-D drift equation [41]. Equations (2.10) are first-order ordinary differential equations with solutions [45]

$$f^{dc}(p_z) = e^{p_z/\Delta p_z} \int_u^{p_z} \frac{-F_0(p_z')}{\Delta p_z} e^{-p_z'/\Delta p_z} dp_z' + f^{dc}(u) e^{(p_z - u)/\Delta p_z}, \tag{2.11a}$$

$$f_0^{ac}(p_z) = e^{\Omega p_z/\Delta p_z} \int_u^{p_z} -R_a \frac{\partial f^{dc}(p_z')}{\partial p_z'} e^{-\Omega p_z'/\Delta p_z} dp_z' + f_0^{ac}(u) e^{\Omega(p_z - u)/\Delta p_z}. \tag{2.11b}$$

In order to find the total distribution given by (2.8), two approaches are followed. The first involves a numerical computation of the integrals by using the exact dispersion relation (2.1) in the Fermi distribution $F_0(\cdot)$. Although accurate, this approach is rather time-consuming. The second, is analytical and uses the approximate linear dispersion relation (2.2) which results in closed form expressions for the DC distribution given by (2.19) and (2.21) and for the AC distribution given by (2.23) and (2.25).

2.3.2.1 Numerical resolution of the BTE

The expressions in (2.11) are implicit for unknown functions appear at both sides of their equal signs, namely $f^{dc}(\cdot)$ in (2.11a) and $f_0^{ac}(\cdot)$ and $f^{dc}(\cdot)$ in (2.11b). They may be transformed into explicit expressions by enforcing the $2u$ periodicity of $f^{dc}(p_z)$ and $f_0^{ac}(p_z)$:

$$f^{dc}(-u) = f^{dc}(u), \tag{2.12a}$$

$$f_0^{ac}(-u) = f_0^{ac}(u). \tag{2.12b}$$

First, applying (2.12a) to (2.11a), it is found that

$$f^{dc}(u) = \frac{e^{-u/\Delta p_z}}{1 - e^{-2u/\Delta p_z}} \int_{-u}^{u} \frac{F_0(p'_z)}{\Delta p_z} e^{-p'_z/\Delta p_z} dp'_z. \tag{2.13}$$

Substituting (2.13) back into (2.11a) yields the explicit and numerically stable form for the DC distribution

$$f^{dc}(p_z) = \int_{p_z}^{u} \frac{F_0(p'_z)}{\Delta p_z} e^{(p_z - p'_z)/\Delta p_z} dp'_z + \frac{e^{(p_z-u)/\Delta p_z}}{1 - e^{-2u/\Delta p_z}} \int_{-u}^{u} \frac{F_0(p'_z)}{\Delta p_z} e^{-(p'_z+u)/\Delta p_z} dp'_z.$$

Following a similar process for the AC distribution, namely, applying (2.12b) to (2.11b), yields

$$f_0^{ac}(p_z) = \int_{p_z}^{u} R_a \frac{\partial f^{dc}(p'_z)}{\partial p'_z} e^{\Omega(p_z - p'_z)/\Delta p_z} dp'_z + \frac{e^{\Omega(p_z-u)/\Delta p_z}}{1 - e^{-2\Omega u/\Delta p_z}} \times \int_{-u}^{u} R_a \frac{\partial f^{dc}(p'_z)}{\partial p'_z} e^{-\Omega(p'_z+u)/\Delta} dp'_z.$$

2.3.2.2 Analytical resolution of the BTE

Analytical expressions for the distributions are obtained under the following two assumptions : 1) linear approximation (2.2) for the dispersion relation and 2) negligible distribution at the limits $\pm u$ of the Brillouin zone so that the periodicity in p_z can be neglected. Instead, the distributions are set to zero at infinity, which greatly simplifies the equations. Furthermore, as a consequence of (2.2), the distributions and the current densities are evaluated separately for positive and negative momentum.

DC Distribution : Proceeding from (2.11a), u is chosen as ∞ and $f^{dc}(\infty)$ is set to 0 following 2) above, yielding

$$f^{dc}(p_z) = e^{p_z/\Delta p_z} \int_{p_z}^{\infty} \frac{F_0(p'_z)}{\Delta p_z} e^{-p'_z/\Delta p_z} dp'_z, \tag{2.14}$$

or

$$f^{dc}(x) = y e^{yx} I(x), \tag{2.15}$$

where $y = (k_B T)/(v_f \Delta p_z)$, $x = (v_f p_z)/(k_B T)$ and

$$I(x) = \int_x^{\infty} \frac{e^{-yx'}}{1 + e^{|x'|}} dx'. \tag{2.16}$$

The function $I(x)$ is computed analytically using the McLaurin series expansion

$$\frac{1}{1 + e^{-x}} = \sum_{n=0}^{\infty} (-1)^n e^{-nx}, \tag{2.17}$$

which holds for any $x > 0$. Subsequently, (2.16) yields for $x > 0$

$$\begin{aligned} I(x_+) &= \int_x^{\infty} \frac{e^{-yx'}}{1 + e^{x'}} dx' \\ &= \int_x^{\infty} \frac{e^{-(y+1)x'}}{1 + e^{-x'}} dx' \\ &= \int_x^{\infty} e^{-(y+1)x'} \sum_{n=0}^{\infty} (-1)^n e^{-nx'} dx' \\ &= \sum_{n=0}^{\infty} \frac{(-1)^n}{y + n + 1} e^{-(y+n+1)x}. \end{aligned} \tag{2.18}$$

and

$$f^{dc}(x_+) = y \sum_{n=0}^{\infty} \frac{(-1)^n}{y + n + 1} e^{-(n+1)x}. \tag{2.19}$$

Similarly (2.16) becomes for $x < 0$

$$
\begin{aligned}
I(x_-) &= \int_x^0 \frac{e^{-yx'}}{1+e^{-x'}}dx' + I(0) \\
&= \int_x^0 \frac{e^{-(y-1)x'}}{1+e^{x'}}dx' + I(0) \\
&= \int_x^0 e^{-(y-1)x'} \sum_{n=0}^{\infty}(-1)^n e^{nx'}dx' + I(0) \\
&= \sum_{n=0}^{\infty}(-1)^n \left\{ \frac{1-e^{(-y+n+1)x}}{-y+n+1} + \frac{1}{y+n+1} \right\}, \qquad (2.20)
\end{aligned}
$$

and

$$
f^{dc}(x_-) = y\sum_{n=0}^{\infty}(-1)^n \left\{ \frac{e^{yx}-e^{x(n+1)}}{-y+n+1} + \frac{e^{yx}}{y+n+1} \right\}. \qquad (2.21)
$$

AC Distribution : Under the same assumptions, (2.11b) transforms to

$$
f_0^{ac}(x) = e^{\Omega yx}\int_x^{\infty} R_a \frac{\partial f^{dc}(x')}{\partial x'} e^{-\Omega yx'}dx'. \qquad (2.22)
$$

For $x > 0$, substituting (2.19) into (2.22), we get

$$
\begin{aligned}
f_0^{ac}(x_+) &= -(R_a y)e^{\Omega yx}\sum_{n=0}^{\infty}\frac{(-1)^n(n+1)}{y+n+1}\int_x^{\infty} e^{-(y\Omega+n+1)x'}dx' \\
&= -(R_a y)\sum_{n=0}^{\infty}\frac{(-1)^n(n+1)}{y+n+1}\frac{e^{-(n+1)x}}{y\Omega+(n+1)}. \qquad (2.23)
\end{aligned}
$$

For $x < 0$, (2.22) becomes

$$
\begin{aligned}
f_0^{ac}(x_-) &= e^{\Omega yx}\left\{ \int_x^0 R_a \frac{\partial f^{dc}(x')}{\partial x'} e^{-\Omega yx'}dx' + \int_0^{\infty} R_a \frac{\partial f^{dc}(x')}{\partial x'} e^{-\Omega yx'}dx' \right\} \\
&= e^{\Omega yx}\left\{ \int_x^0 R_a \frac{\partial f^{dc}(x')}{\partial x'} e^{-\Omega yx'}dx' + f_0^{ac}(0) \right\}. \qquad (2.24)
\end{aligned}
$$

Substituting (2.21) and $f_0^{ac}(0)$ from (2.23) into (2.24) we get

$$f_0^{ac}(x_-) = (R_a y)\sum_{n=0}^{\infty}(-1)^n \times \Bigg[\left(\frac{e^{x(n+1)} - e^{y\Omega x}}{-y\Omega + n + 1}\right)\left(\frac{n+1}{-y+n+1}\right) - \left(\frac{e^{yx} - e^{y\Omega x}}{1-\Omega}\right)\left(\frac{1}{y+n+1} + \frac{1}{-y+n+1}\right) - \left(\frac{e^{y\Omega x}}{\Omega + n + 1}\right)\left(\frac{n+1}{y\Omega + n + 1}\right)\Bigg]. \tag{2.25}$$

2.3.2.3 Results and comparison

The DC distribution function is calculated through numerically through (2.14) and analytically through (2.19) and (2.21). The results are plotted in Fig. 2.4. At relatively low-fields, the distribution is a symmetric gaussian curve, shifted slightly to the negative momentum thereby conducting current. This is in accordance with the low-field approximation which approximates the distribution to $f^{dc}(p_z + \Delta p_z)$ [41]. At increasingly higher fields ($E_z^{dc} > 10^4$ V/m), the distribution of the electrons spreads out across the negative momentum, acquiring an exponentially decreasing tail. Good agreement between the numerical and analytical solutions is found at all fields.

Less trivial, the magnitude of the AC distribution f_0^{ac} at different fields is plotted in Fig. 2.5. The numerical and analytical solutions agree as well.

2.3.3 Surface current density

The surface current density along an 2-D sheet is given by [9]

$$J_z^{dc,ac} = \frac{-4e}{(2\pi\hbar)^2}\iint_{BZ} f^{dc,ac}(p_z, p_\phi) v_z(p_z, p_\phi) dp_z dp_\phi, \tag{2.26}$$

where the integration is performed over $\mathrm{BZ}_{Slepyan}$ (Sec. 2.3.1). The factor 4 in (2.26) accounts for the twofold spin degeneracy as well as the equal contribution from electrons in the conduction band and holes in the valence band. In zigzag CNTs, the azimuthal momentum p_ϕ is quantized as $p_\phi = (2\pi\hbar s)/(\sqrt{3}na_{cc})$ due to transversal confinement [4]. Equation (2.26) becomes then

$$J_z^{dc,ac} = \frac{-4e}{(2\pi\hbar)^2}\frac{2\pi\hbar}{\sqrt{3}na_{cc}}\sum_{s=1}^{n}\int_{-u}^{u} f^{dc,ac}(p_z, s) v_z(p_z, s) dp_z. \tag{2.27}$$

The current density is also found through both numerical and analytical means from the corresponding distributions. In the numerical approach, the integral in (2.27) is computed

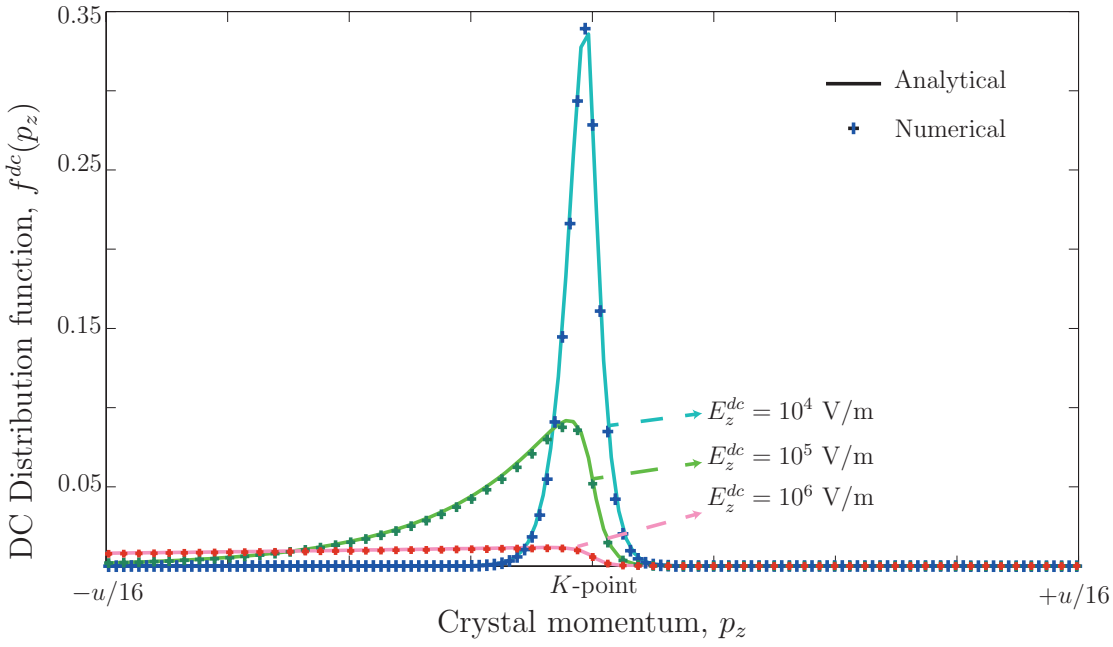

Figure 2.4 Comparison of the analytical and numerical solutions for the DC distribution function.

numerically for all the subbands.

2.3.3.1 Analytical derivation of the current density

The analytical form of the current density along zigzag CNTs may be found from (2.27) by only considering the contribution due to the subbands crossing the Fermi energy, which in BZ are $s = q, 2q$. Furthermore, noting that the dispersion bands $s = q, 2q$ are equivalent as seen from Fig. 2.2, the linear approximation to the energy dispersion, (2.2), is doubly degenerate. Thus, (2.27) becomes

$$J_z^{dc,ac} = \frac{-4e}{\sqrt{3}na_{cc}\pi\hbar}\int_{-u}^{u} f^{dc,ac}(p_z)v_z(p_z)dp_z, \tag{2.28}$$

where the $2q$ argument is dropped since only one band exists. Within the linear approximation (2.2), $v_z(p_z) = v_f\frac{|p_z|}{p_z}$ and (2.28) becomes

$$J_z^{dc,ac} = \frac{-4ev_f}{\sqrt{3}na_{cc}\pi\hbar}\int_{-u}^{u} \text{sign}(p_z)f^{dc,ac}(p_z)dp_z, \tag{2.29}$$

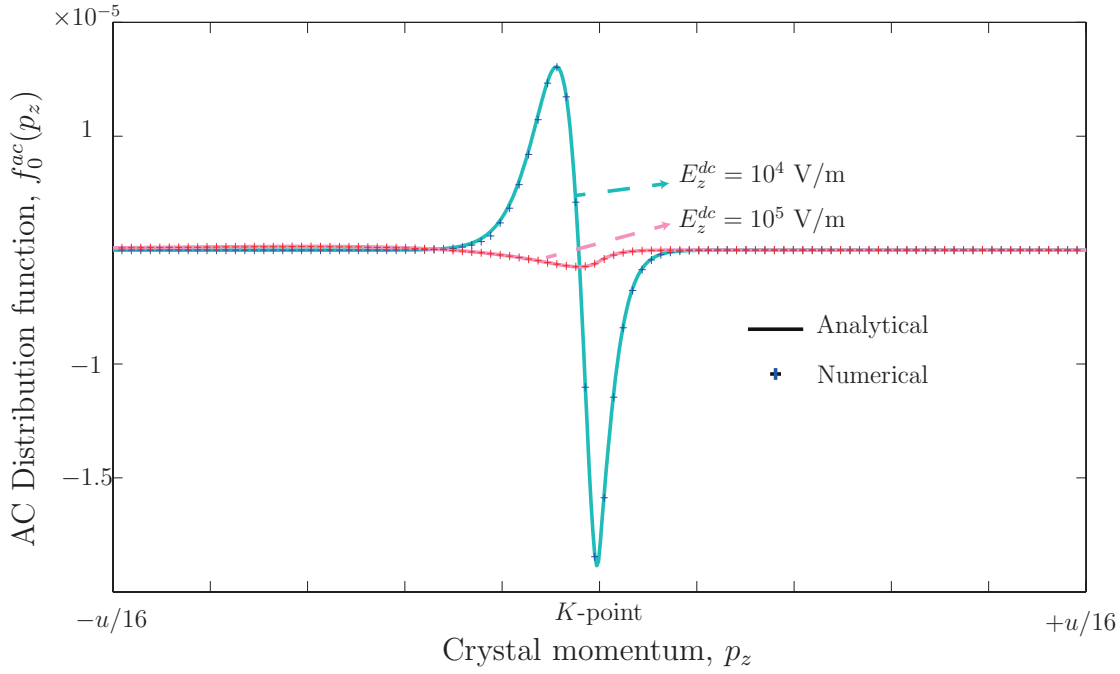

Figure 2.5 Comparison of the analytical and numerical solutions for the AC distribution function.

Letting

$$j_{\pm}^{dc,ac} = \int_0^{\pm u} f^{dc,ac}(p_z) dp_z, \tag{2.30}$$

(2.29) is re-written as

$$J_z^{dc,ac} = \frac{-4ev_f}{\sqrt{3}na_{cc}\pi\hbar} \left(j_-^{dc,ac} + j_+^{dc,ac} \right). \tag{2.31}$$

Substituting (2.19) and (2.21) into (2.30),

$$j_+^{dc} = y \sum_{n=0}^{\infty} \frac{(-1)^n}{y+n+1} \frac{1 - e^{-(n+1)v}}{n+1}, \tag{2.32a}$$

$$j_{-}^{dc} = -y\sum_{n=0}^{\infty}(-1)^n\left\{\frac{1}{y(n+1)} + \frac{1}{y(y+n+1)} + \frac{e^{-yv}}{y}\left[\frac{1}{y+n+1} + \frac{1}{-y+n+1}\right]\right\},$$

where $v = 2\pi\hbar v_f/(3a_{cc}k_BT)$. Similarly, substituting (2.23) and (2.25) into (2.30),

$$j_{0+}^{ac} = (-R_a y)\sum_{n=0}^{\infty}\frac{(-1)^n}{y+n+1}\frac{1-e^{-(n+1)u}}{y\Omega+n+1}, \tag{2.33a}$$

$$\begin{aligned} j_{0-}^{ac} =& (-R_a y)\sum_{n=0}^{\infty}(-1)^n\left\{\frac{1-e^{-(n+1)v}}{(-y+n+1)(-y\Omega+n+1)}\right. \\ &- \left(\frac{n+1}{-y+n+1}\frac{1}{-y\Omega+n+1} + \frac{n+1}{y+n+1}\frac{1}{y\Omega+n+1}\right)\frac{1-e^{-y\Omega v}}{y\Omega} \\ &\left. + \frac{1}{1-\Omega}\left(\frac{1}{y+n+1} + \frac{1}{y+n+1}\right)\frac{1-\Omega-e^{-y\Omega v}+\Omega e^{-yv}}{y\Omega}\right\}. \end{aligned} \tag{2.33b}$$

2.3.3.2 Results and comparison

Figure 2.6 plots the DC current versus the applied DC field. The linear approximation calculation starts deviating significantly from the tight-binding one at fields higher than 10^5 V/m. At such high fields, the electrons populate higher energies in the dispersion diagram, where the difference between (2.1) and (2.2) is large, as it is seen in Fig. 2.2. Nevertheless, even at such high fields, the approximate analytical solution presents a very good qualitative agreement with the exact numerical one.

The slope inversion of the current curve at high fields reveals the existence of an NDC region, which was previously reported in [19]. The threshold field value at which this NDC occurs is found to be around 3×10^5 V/m and 5×10^5 V/m for the numerical and analytical solutions, respectively. This NDC is caused by the same underlying physical mechanism seen in semiconductor superlattices [46], as shall be discussed in Sec. 2.6.

The AC conductivity, defined as $\sigma^{ac}(E_z^{dc}) = J_z^{ac}(E_z^{dc})/E_z^{ac}$, is plotted in Fig. 2.7(a) for $E_z^{ac} = 1$ V/m at a frequency of 1 GHz. Again, a reasonable agreement between the linear approximation and the numerical solution is found. Henceforth, we use the analytical approximation in the remainder of the paper. A region of absolute negative AC conductivity is found at high DC fields, apparent in Fig. 2.7(b).

Fig. 2.8 plots σ_z^{ac} versus frequency for different E_z^{dc} values. Negative AC conductivity values ($E_z^{dc} > 5\times10^5$ V/m) tend to an oscillating positive value at frequencies greater than 30 GHz, a response typical of Bloch oscillating electrons [Sec. 2.6].

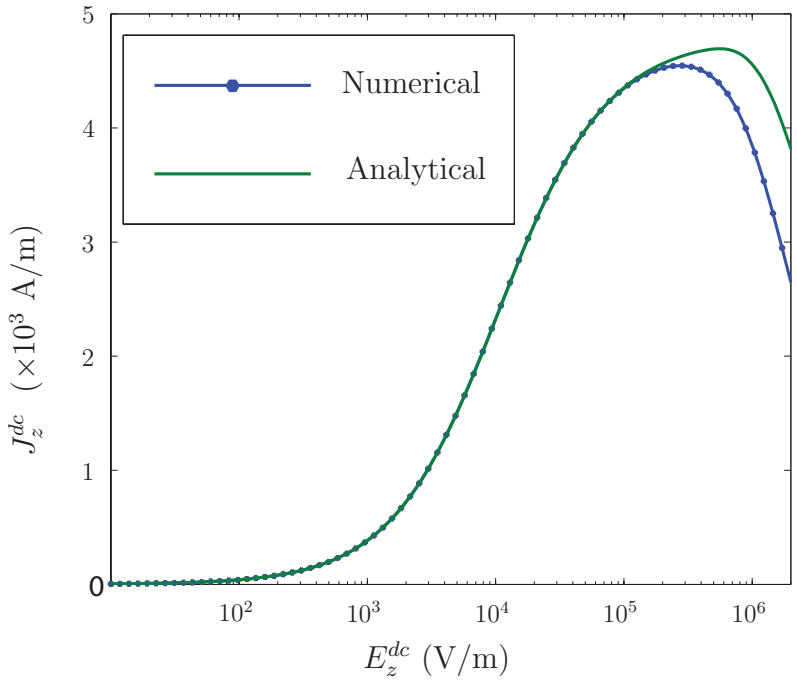

Figure 2.6 DC Current density of a $(9, 0)$ zigzag CNT versus the applied DC electric field, computed numerically by (2.27) via (2.14) and analytically by (2.32). NDC is observed at fields higher than 10^5 V/m.

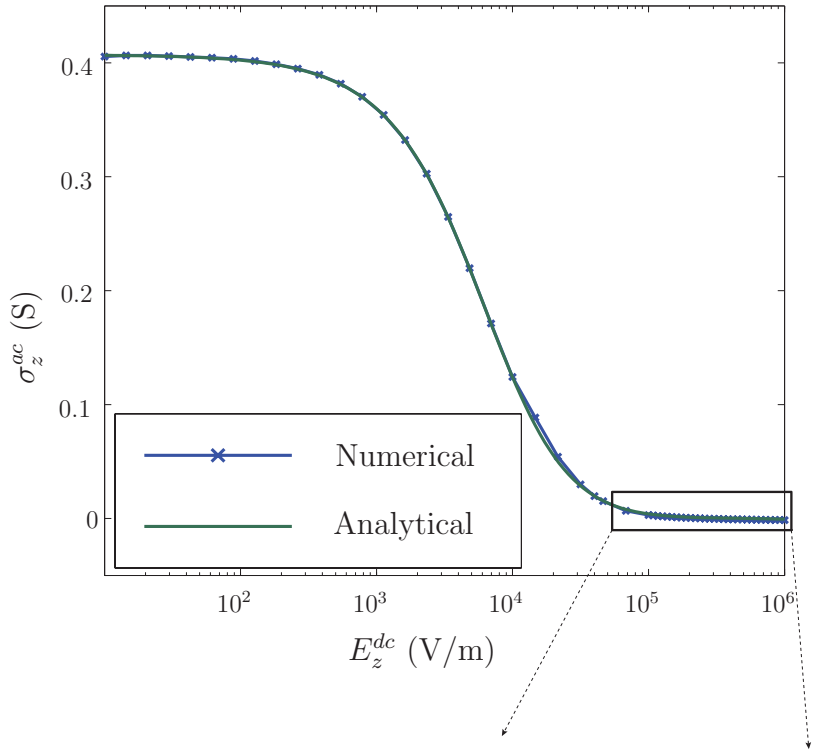

(a)

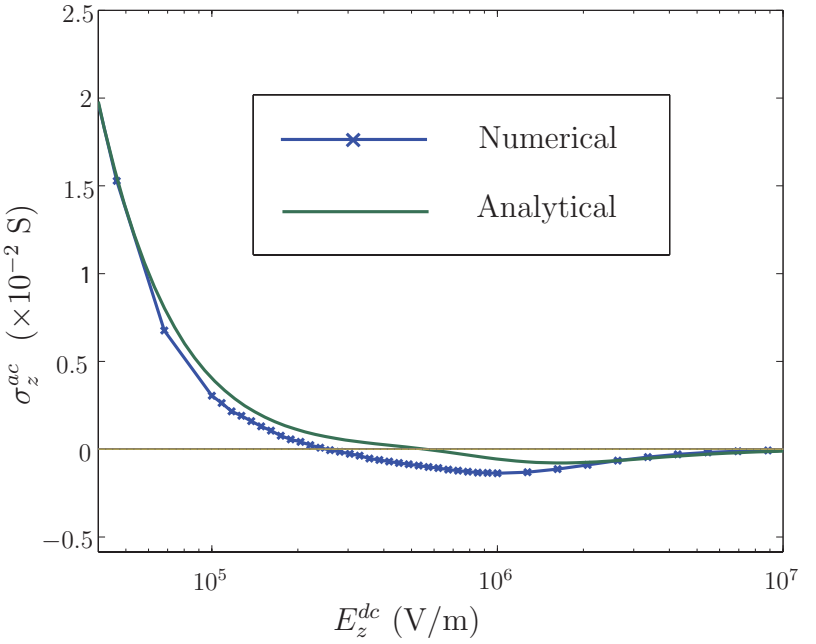

(b)

Figure 2.7 AC Conductivity of a $(9, 0)$ zigzag CNT versus the DC field at 1 GHz, computed numerically by (2.27) via (2.14) and analytically using (2.33). (a) Wide view (b) Zoom on the region of absolute negative conductivity.

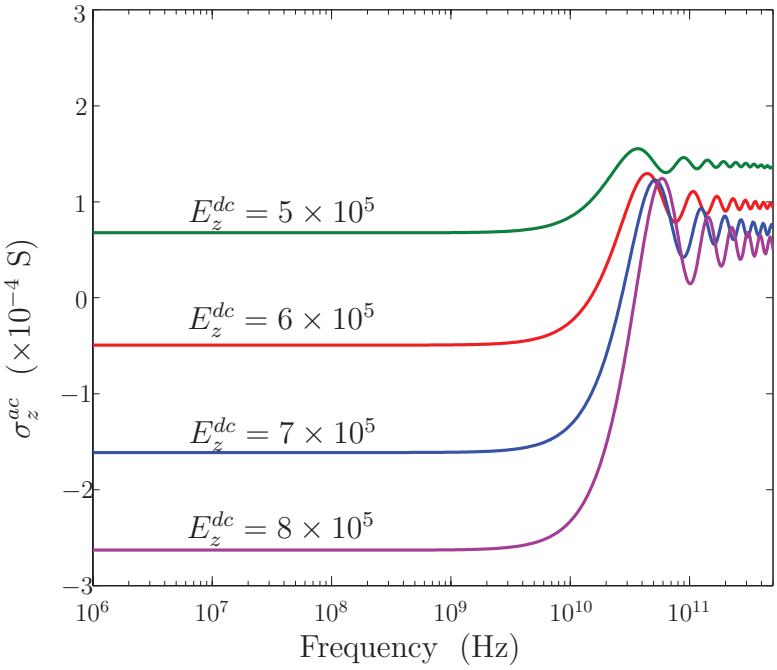

Figure 2.8 AC Conductivity, computed using (2.33), for a (9,0) CNT exposed to different values of DC field versus the frequency.

2.4 Electromagnetic problem

Electromagnetic wave propagation along cylindrical single-conductors is typically described by a Sommerfeld surface wave mode possessing no axial magnetic field H_ϕ (TM_z). It is considered to be a surface wave due to the attachment of the wave to the surface. However, the larger the metal conductivity, the lighter the attachment and, in the limit of infinite conductivity, the wave does not couple to the conductor [47].

In Appendix A, the solution of Maxwell's equations for a *full* cylindrical conductor is presented. A consequent eigenmode solution of the electromagnetic dispersion in a copper wire helps elucidate the reason behind the immense slow-wave nature of CNTs. Here, the electromagnetic solution is presented for the *hollow* cylindrical conductor with vanishing wall thickness, and the boundary conditions are applied to yield a relation for the AC current density $J^{ac}_{\mathrm{Maxwell}}$.

2.4.1 Surface wave mode (TM_z) for a hollow cylindrical conductor

The problem of surface-wave propagation along a hollow circular conducting tube with zero conductor thickness, like the considered metal zigzag CNT, can be solved in terms of the Hertz vector potential [47]. The electric and magnetic fields of the dominant mode of this structure, which is also an azimuthally symmetric TM_z mode [40], take the form [48]

$$\mathbf{E^{ac}} = \nabla \times \nabla \times \mathbf{\Pi_e} = \nabla(\nabla \cdot \mathbf{\Pi_e}) + k_0^2 \mathbf{\Pi_e}, \tag{2.34a}$$

$$\mathbf{H^{ac}} = -j\omega\epsilon_0(\nabla \times \mathbf{\Pi_e}), \tag{2.34b}$$

where,

$$\mathbf{\Pi_e} = \hat{z}e^{j(hz-\omega t)} \begin{cases} A_- I_0(\gamma\rho)K_0(\gamma R) & \text{for } \rho < R \\ A_+ I_0(\gamma R)K_0(\gamma\rho) & \text{for } \rho > R \end{cases}. \tag{2.35}$$

In (2.35) A_- and A_+ are the amplitudes inside and outside the tube, respectively, R is the CNT radius (Fig. 2.1), ρ is the radial distance, $I(\cdot)$ and $K(\cdot)$ are the modified Bessel functions of the first kind and the second kind, respectively, γ is the transverse wavenumber, related to the axial wavenumber h and the free space wavenumber k_0 through $\gamma^2 = h^2 - k_0^2$.

The electric and magnetic fields satisfy the boundary conditions

$$\lim_{\delta\to 0}\left[E^{ac}_\phi|_{\rho=R+\delta} - E^{ac}_\phi|_{\rho=R-\delta}\right] = 0, \tag{2.36a}$$

$$J^{ac}_z = \lim_{\delta\to 0}\left[H^{ac}_\phi|_{\rho=R+\delta} - H^{ac}_\phi|_{\rho=R-\delta}\right], \tag{2.36b}$$

respectively, the former of which expresses the continuity of the tangential electric field across the surface of the tube, while the latter relates the tangential magnetic field to the surface current density J_z^{ac} along the tube.

Substituting (2.35) into (2.34a), and then inserting the result into (2.36a), gives $A = A_- = A_+$. Similarly, substituting (2.35) into (2.34b), and then inserting the result into (2.36b), yields

$$\begin{aligned} J_z^{ac} &= -j\omega\epsilon A\gamma[I_0(\gamma R)K_1(\gamma R) + I_1(\gamma R)K_0(\gamma R)]e^{j(hz-\omega t)} \\ &= -j\frac{\omega\epsilon_0 A}{R}e^{j(hz-\omega t)}. \end{aligned} \tag{2.37}$$

Furthermore, inserting (2.35) into (2.34a), the longitudinal electric component is found as

$$E_{z0}^{ac} = E_z^{ac}(\rho = R) = A(k^2 - h^2)I_0(\gamma R)K_0(\gamma R)e^{j(hz-\omega t)}. \tag{2.38}$$

Finally, substituting the expression for A found from this relation into (2.37) yields the dominant TM_z mode surface current density

$$J_z^{ac} = j\frac{\omega\epsilon_0 E_{z0}^{ac}}{R\gamma^2 I_0(\gamma R)K_0(\gamma R)}e^{j(hz-\omega t)}. \tag{2.39}$$

The electromagnetic dispersion relation in this expression, $h(\omega)$, which is needed for the investigation of possible amplification, is not determined yet at this point, since J_z^{ac} is still unknown. It will be fully determined by consistently including the information on the properties of the CNT material via the BTE current solution (2.27) in the next section.

2.5 Electromagnetic dispersion : eigensolution

The solution for the complete transport-electromagnetic problem of the traveling-wave CNT (Fig. 2.1) is obtained by equating the current found through the solution of the BTE to the one found through the solution of Maxwell's equations, i.e.

$$(J_z^{ac})_{\text{BTE}} = (J_z^{ac})_{\text{Maxwell}}\,, \tag{2.40}$$

where $(J_z^{ac})_{\text{BTE}}$ and $(J_z^{ac})_{\text{Maxwell}}$ were found using (2.27) and (2.39), respectively. Substituting (2.27) and (2.39) into (2.40) yields a transcendental equation in the complex propagation factor

$$h(\omega) = \beta(\omega) - j\alpha(\omega), \tag{2.41}$$

where $\beta(\omega)$ and $\alpha(\omega)$ are the phase factor and the attenuation factor, respectively. We solved (2.40) via the Muller's complex root finding method to find $h(\omega)$.

The electromagnetic dispersion will be given in the absence of a biasing DC field at first. Later, the dispersion will be given with respect to an applied DC field.

2.5.1 No DC field

In the limit of zero DC applied field, α and β were verified to agree with the results in [2], which addresses the problem in the absence of DC field. For this purpose,

$$\lim_{E_z^{dc}\to 0} (J_z^{ac})_{\text{BTE}} = (J_z^{ac})_{\text{Maxwell}} \tag{2.42}$$

the eigensolution of the propagation factor $h(\omega)$ is plotted in Fig. 2.9 for three different CNTs. The CNTs were all chosen to be metallic zigzag CNTs with increasing radii. Figure 2.9 shows that β and α increase with increasing radius of CNTs. At frequencies below 10 GHz, α is to same order as β noting a quick attenuation of the wave in this band. However, the gap between α and β widens signaling a better propagation for frequencies beyond 10 GHz.

Then, using $v_p(\omega) = \omega/\beta(\omega)$, we plot the phase velocity with respect to frequency in Fig. 2.10. The results agree well with [2] with $v_p \approx 10^6$ m/s around 1 GHz. Figs A.1 and A.2 in Appendix A plot the same variables for a copper wire with different radii, calculated using the Sommerfeld solution [49; 50]. As is especially noticeable from Fig. A.2, the phase velocity decreases significantly with a decrease in the radius below the skin depth (1 μm at 1 GHz). However, comparing 2.10 with A.2 it can be seen that the phase velocity is significantly lower in a CNT. Such a pronounced slow-wave factor can be attributed to the infinitesimal thickness of the CNT walls.

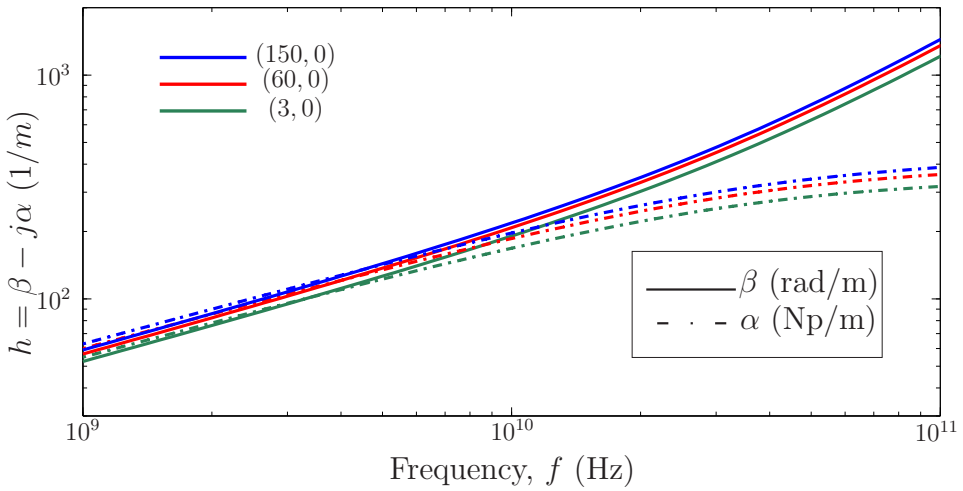

Figure 2.9 Electromagnetic dispersion relation $h(\omega) = \beta(\omega) - j\alpha(\omega)$ (2.41) of a metallic zigzag CNT with respect to frequency, calculated with $E_z^{dc} = 0$.

2.5.2 RF and DC : traveling-wave amplification

Fig. 2.11 plots the electromagnetic dispersion relation $h(\omega)$ (2.41) found using Muller's method at 1 GHz while sweeping the DC field. For $E_z^{dc} < 3 \times 10^5$ V/m, both the magnitude of the attenuation factor and the slow-wave factor β/k_0 increase as E_z^{dc} increases. At the threshold field of the negative differential DC conductivity (Fig. 2.6), the attenuation factor changes sign, which leads to an exponentially growing wave, and indicates that the surface-wave mode is amplified. Amplification was expected due to the negative AC conductivity found in sec. 2.3.3.2. The wave was amplified for frequencies up to 10 GHz, similar to the range of negative AC conductivity which is shown in Fig. 2.8

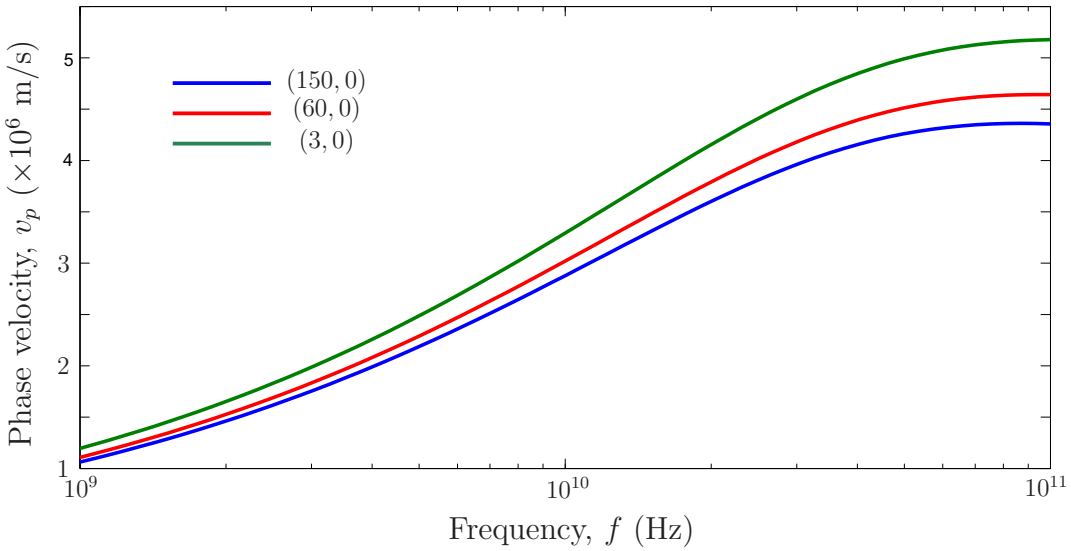

Figure 2.10 Phase velocity $v_p(\omega) = \omega/\beta(\omega)$ of the traveling surface waves along a metallic zigzag CNT with respect to frequency, calculated with $E_z^{dc} = 0$.

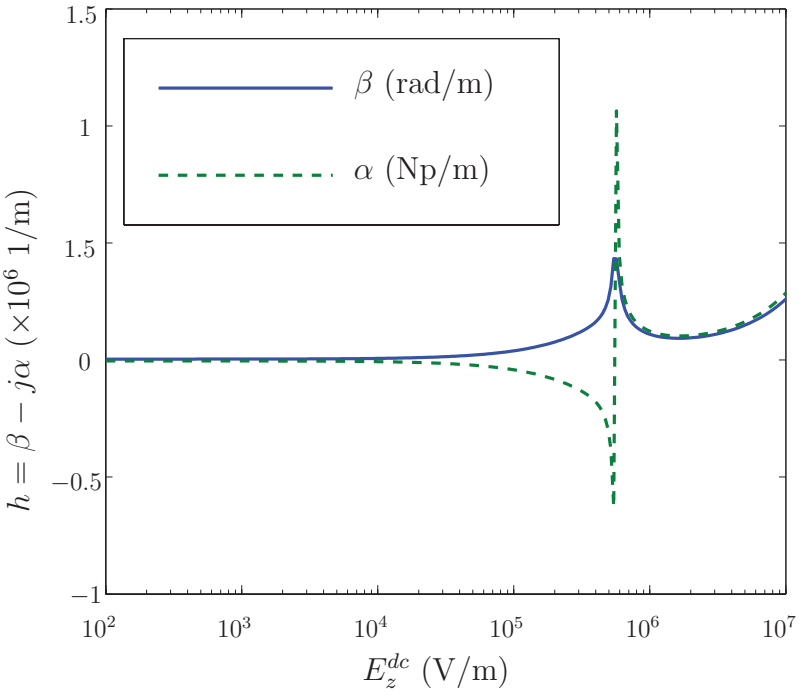

Figure 2.11 Electromagnetic dispersion relation $h(\omega) = \beta(\omega) - j\alpha(\omega)$ (2.41) of a (9,0) CNT exposed to a DC electric field E_z^{dc}, found by solving (2.40) at 1 GHz.

2.6 Discussion

2.6.1 Physical mechanism for amplification

The initial motivation for solving the problem of a CNT under simultaneous AC-DC fields was to investigate the possibility of a traveling-wave amplification similar in its mechanism to that of the vacuum-based TWTs [3]. Namely, the mechanism for such an amplification in TWTs, as stated in sec. 1.4.1.1, is the phase and drift velocity synchronization. In the problem at hand, the drift velocity is given by [41]

$$v_d = \frac{\int v_z(p_z) f^{dc}(p_z) dp_z}{\int f^{dc}(p_z) dp_z}. \tag{2.43}$$

Figure 2.12 plots the comparison between the drift and phase velocities with respect to applied DC field, E_z^{dc}. Despite the velocities being equal at a field of $E_z^{dc} = 10^4$ V/m, the drift velocity is two orders of magnitude greater than the phase velocity of the amplified mode at $E_z^{dc} = 5 \times 10^5$ V/m. Therefore, it can not be concluded at this point that a mechanism similar in its origins to TWTs is behind the amplification in our analysis.

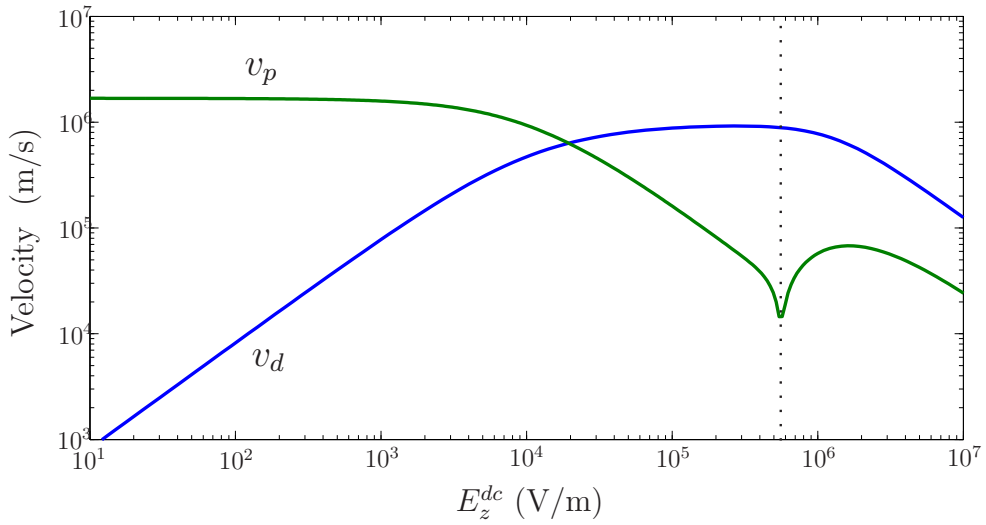

Figure 2.12 Comparison between the drifting velocity of the electrons, v_d, and the phase velocity of the traveling waves, v_p. As it can be seen, there is no match of velocity (ie. synchronization) at fields leading to amplification, $E_z^{dc} = 3 \times 10^5$ V/m.

On the other hand, as shown in Fig. 2.13, as the DC bias increases, the electron distribution is non-zero at the BZ edges. The fact that charge carriers are driven by a strong DC field beyond the Bragg point at the BZ edge where they undergo an inversion of group

velocity direction (Fig. 2.13) evidently shows that the reason behind NDC and amplification is the phenomenon known as Bloch oscillations [51].This can be physically understood as Bragg reflections occurring when the electron wavelength is comparable to twice the lattice period. In the presence of inelastic scattering, Esaki and Tsu showed, for the case of semiconductor superlattices, that Bloch oscillations yield a negative differential conductivity [46]. Furthermore, it was shown by Ktitorov *et al.* [52] that superimposing an AC-field yields a negative AC conductivity below the Bloch frequency, given by $\omega_B = aeE_z^{dc}/(2\hbar)$, where a is the lattice constant [51]. In the present work, when $E_z^{dc} = 3 \times 10^5$ V/m, the Bloch frequency is $\omega_B \approx 30$ GHz, which agrees very well with the trend seen in Fig. 2.8. Hence, we deduce that the NDC and traveling-wave amplification observed in our model are results of Bloch-type oscillations.

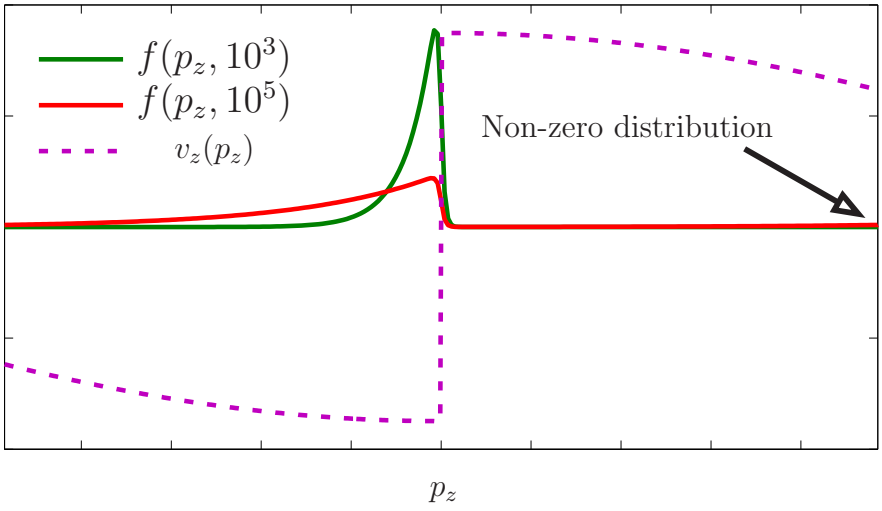

Figure 2.13 Distribution function for two different E_z^{dc}, superimposed with the corresponding group velocity v_z, all with respect to the momentum. The distribution of the electrons at the edges of the BZ is non-zero signaling a Bloch-type oscillation.

2.7 Spatial disperion (non-local effects)

In sec. 2.3.2, we neglected spatial dispersion by setting $h = 0$ whilst solving the BTE. The reasoning behind the assumption was the presumed negligible length of the mean free path with respect to the guided wavelength. However, as is noticeable in fig. 2.12, the phase velocity is slowed down by a factor of 10^2 to 10^3, therefore the guided wavelength is shortened down to an order of tens of microns at GHz frequencies. This development hints at the possibility

of neglecting potentially important non-local effects. Here, a preliminary solution of the non-local problem is presented. By including the spatial variation h in the assumed distribution form as in (2.7), (2.9) becomes

$$j(hv_z - \omega)f^{ac} - e(E_z^{dc} + E_z^{ac})\frac{\partial(f^{dc} + f^{ac})}{\partial p_z} = -\frac{f^{dc} + f^{ac} - F_0}{\tau}. \tag{2.44}$$

The DC solution remains the same, while the AC distribution no longer can be solved with h unknown at this point. The AC current density, found using (2.26), thus becomes a function of h. Again, (2.40) is solved by sweeping E_z^{dc} and using Muller's method to find the allowed values of h in the complex plane. By considering spatial dispersion, many new modes have emerged as solution to the problem. Distinguishing between different modes as E_z^{dc} is swept requires complex plane analysis, which has not been completed at the time of writing. Therefore, the results plot all the individual solutions found at each sampling point E_z^{dc} in the complex plane. However crude, the current data provide interesting results.

Figs. 2.14 and 2.15 plot $\beta(E_z^{dc})$ and $\alpha(E_z^{dc})$ solutions of the positive propagating modes ($\beta > 0$) at 1 GHz. The previous local results are included in the figures for comparison. The local modes appear to agree with one of the non-local modes. More interestingly, however, fig. 2.15 shows the appearance of an amplified mode ($\beta, \alpha > 0$) around $E_z^{dc} = 10^4$ V/m. This low threshold field coincides with that at which the drift and phase velocities are equal (2.12). Furthermore, the amplification seems to be sustained for larger fields where $v_p < v_d$. Such mode amplification, unlike the one found at fields beyond $E_z^{dc} = 5 \times 10^5$ V/m, is reminiscent of the amplification characteristics in TWTs. This prediction of amplification at such low fields is very promising and deserves further investigation.

2.7.1 Scattering model

The present study utilizes the RTA as the scattering model in the BTE, which assumes a constant scattering time, which is generally considered a good approximation at sufficiently low fields. However, the RTA is known to fail in providing a quantitatively accurate description of transport at high fields [41], when optical phonon emissions begin to affect the scattering time [17]. Furthermore, interband scattering, neglected in our model, becomes more probable at high fields. A further study will apply a more accurate scattering model taking into consideration the energy- and momentum-dependent scattering time [53].

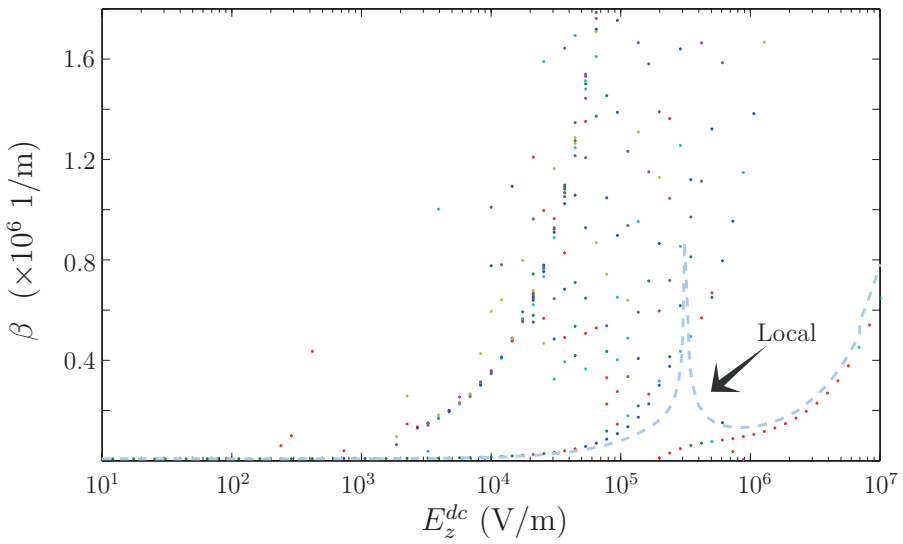

Figure 2.14 The positive propagation constants $\beta > 0$ of the non-local solutions to (2.40) compared to the local case. Without proper complex plane analysis, it is difficult to distinguish between two respective modes.

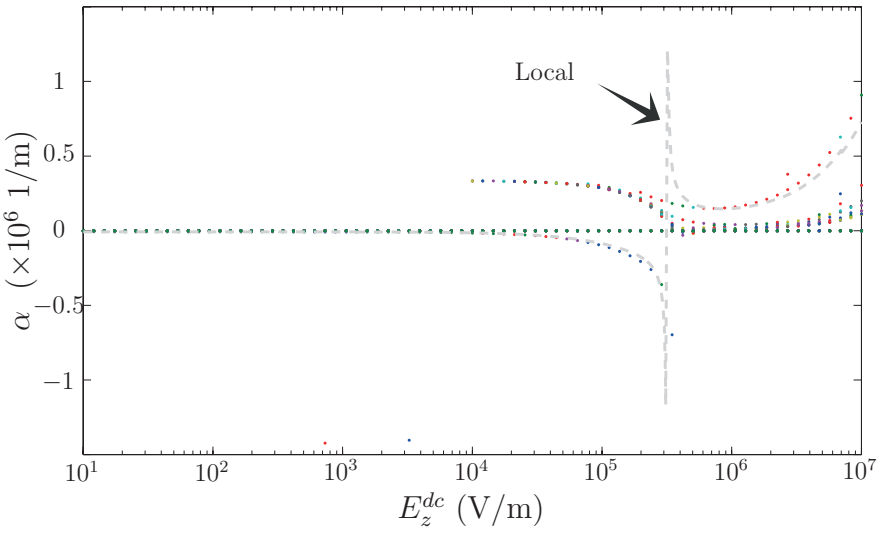

Figure 2.15 The attenuation constant α of the non-local modes (with $\beta > 0$) compared with the local case. Taking spatial dispersion into account leads to an amplification at much lower fields around $E_z^{dc} = 10^4$ V/m.

2.8 Conclusion

We theoretically investigated the possibility of traveling-wave amplification in CNTs. The AC conductivity of a metallic CNT exposed to an axial DC field was computed by solving the BTE within the RTA. Closed-form expressions for the DC and AC current density under the linear approximation of the dispersion relation were derived and they were shown to be in excellent agreement with the numerically computed current density using the tight-binding dispersion relation. Both negative differential DC conductivity and negative AC conductivity were found for DC fields above a threshold field of 5×10^5 V/m and up to frequencies of several tens of GHz. By coupling the BTE to Maxwell's equations, the propagation of a surface wave along a CNT under AC-DC fields was quantitatively described by both neglecting and including spatial dispersion. Hints of traveling-wave amplification were found in both cases, showing promise in the possibility of using CNTs to amplify RF waves when they are biased with a DC field.

CHAPTER 3

Fabrication of Characterization Fixture

3.1 Introduction

The predicted slow-wave propagation, NDC, and traveling-wave amplification in CNTs certainly motivate an experimental study to verify these properties. However, the 1-D nature of CNTs has made their characterization a tedious task. Besides the obvious difficulty that lies in CNT manipulation, there exists an inherent impedance mismatch at RF frequencies between CNTs and the macro-world through which they are probed. The reason for this is the high impedance of CNTs. The transmission line model reported in [26] and described in section 1.3.1.2 yields a CNT characteristic impedance of $Z_{CNT} \approx 6.25K\Omega$, assuming ballistic conduction. Figure 3.1 illustrates this impedance mismatch resulting in the reflection of most of the energy and thus creates a necessity for ultra sensitive and accurate measurement fixtures and techniques. To meet the future goal of experimentally verifying the theory presented in the previous chapter, significant efforts needed to be made to design and fabricate the characterization fixture, which shall be presented in this chapter.

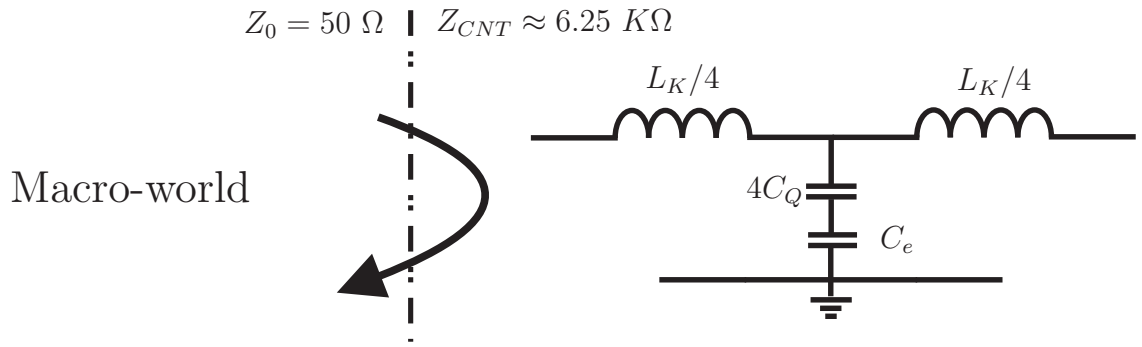

(a)

Figure 3.1 Illustration depicting the inherent mismatch between CNTs and the macro-world.

The overall electromagnetic wave-guiding structure and the contact method are described first. Then, the detailed fabrication procedure and its outcomes are presented. Finally, the conclusion concentrates on the corrections and improvements that could be done in the near future.

3.2 Description of characterization fixture

3.2.1 Electromagnetic waveguiding structure

There has been numerous efforts to characterize the RF properties of CNTs in the literature, most of which using the coplanar waveguide (CPW) as the structure of choice [29; 30; 31]. One reason for this is the planar nature of CPWs which can be designed and fabricated with feature sizes less than a micrometer thanks to modern microfabrication facilities and techniques. Another reason lies in the fact that CPWs can be used to guide much higher frequencies than other planar structures can handle (eg. microstrips) [54].

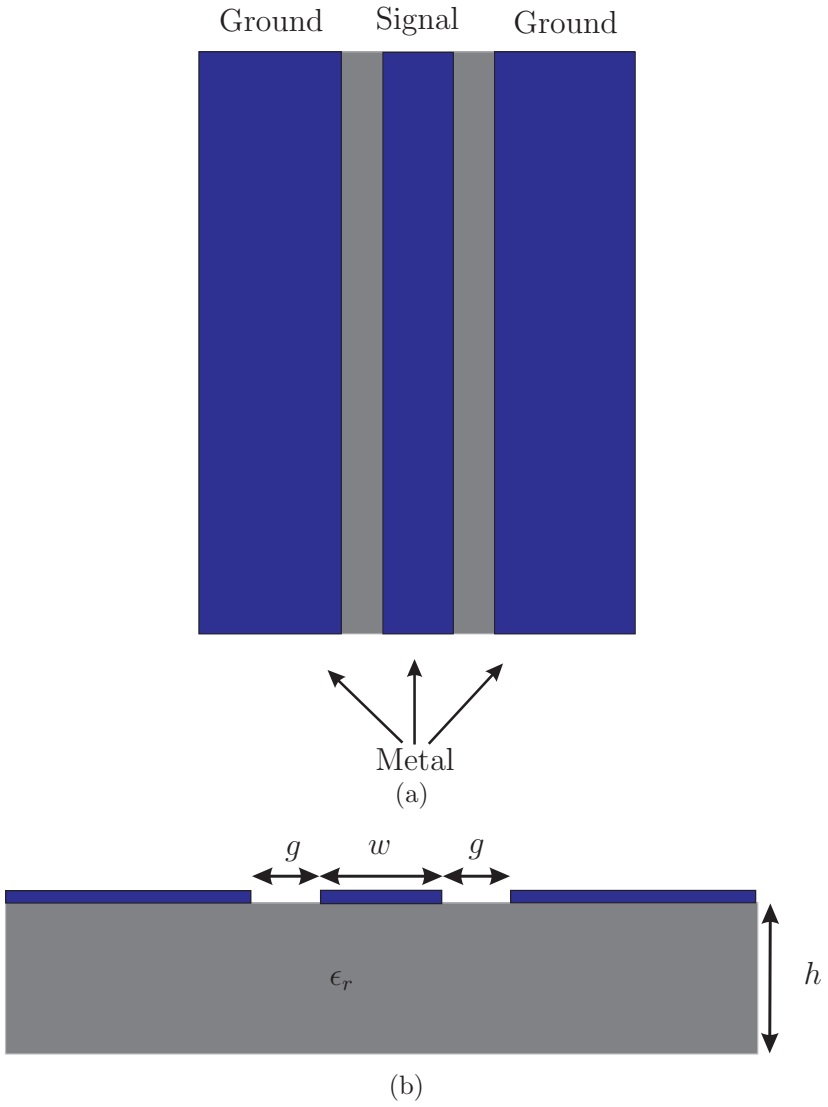

Figure 3.2 Regular ungrounded CPW. View from (a) top and (b) end side.

CPWs mainly consist of three parallel strips of metal on a dielectric substrate as is shown

in Fig. 3.2. The impedance and propagation factor along the structure are directly correlated with the width of the middle strip w, the gap between the lines g, the thickness of the substrate h, and its corresponding relative permittivity ϵ_r. CPWs can carry two fundamental quasi-TEM modes illustrated in Fig. 3.3 : even and odd [54]. The strips on both sides are usually grounded to excite the less dispersive even mode while the middle strip's potential is alternated. The wave is launched across the CPW using trustworthy transitions from coaxial lines (GSG probes). As is with regular microwave transmission lines, CPWs are usually designed to exhibit a standard characteristic impedance of $Z_c = 50\ \Omega$ to allow proper matching with the GSG probes.

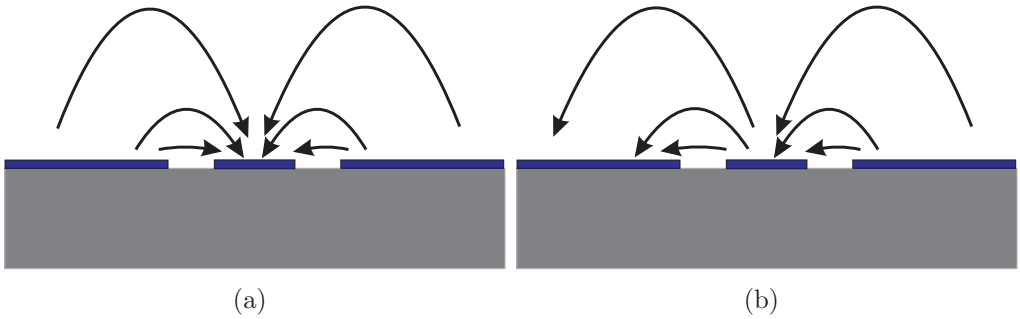

Figure 3.3 Illustration showing the electric field lines in the fundamental modes of the CPW : (a) even mode and (b) odd mode.

In our design, a gap in the central strip allows for CNT(s) to be aligned across for characterization and transport measurements. Furthermore, the width of the strip is tapered down to achieve a much narrower strip. Such tapering serves two goals :

1. Restrict the number of CNTs that can be aligned across the tube.
2. Increase the characteristic impedance of the CPW and therefore slightly decreasing the huge impedance mismatch at the CPW-CNT contact.

The main structure and gap dimensions are shown in Fig. 3.4. The trace and gap width are $w = 100$ and $g = 60\ \mu$m respectively. The trace is tapered down to 2 μm wide to accommodate for very few tubes across, ideally one. Due to the constraint of the CNT lengths, the CPW gap size was consequently chosen to be 1.5 μm. Therefore, there was a need to design an optical lithography mask which has a feature size around 1 μm.

3.2.1.1 TRL calibration

To solve the problem of impedance mismatch and single out the response of the CNT(s) across the gap, a calibration technique will be used to de-embed the unwanted measurements

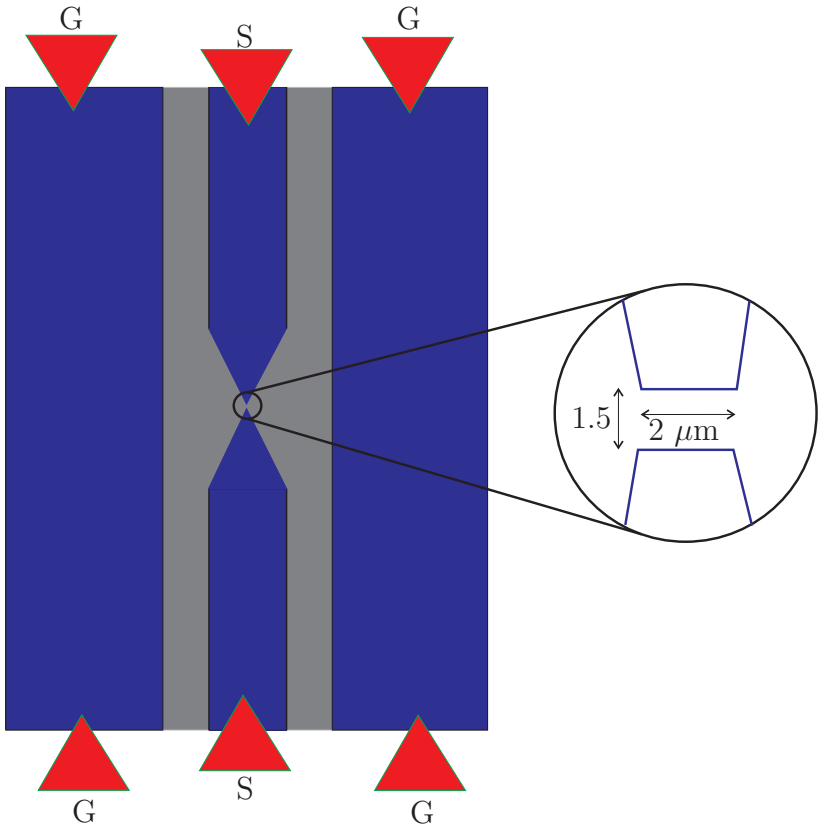

(a)

Figure 3.4 Characterization fixture setup showing the GSG probes, the tapered CPW, and the gap where the CNT should be aligned across.

such as fringe capacitance and phase shift in the CPW. For this purpose, a known and accurate method, namely the Thru-Reflect-Line (TRL)[55], is used. TRL requires the fabrication of three structures. Depicted in Fig. 3.5, they consist of :

- THRU - consists of a straight CPW with no gap.
- REFLECT - open or short ended CPW to achieve a large reflection.
- LINE - consists of a THRU inserted with a 90 degrees transmission line.

Application of a subsequent mathematical technique leads to the extraction of the unwanted measurements. However, since the measurements are outside the scope of this thesis, description of the mathematical technique will left out.

3.2.2 CNT contact

Achieving a good contact to CNTs is a crucial step for fabrication. Figure 3.6 illustrates the possible layouts : top and bottom contact. In the latter option, researchers lay down the

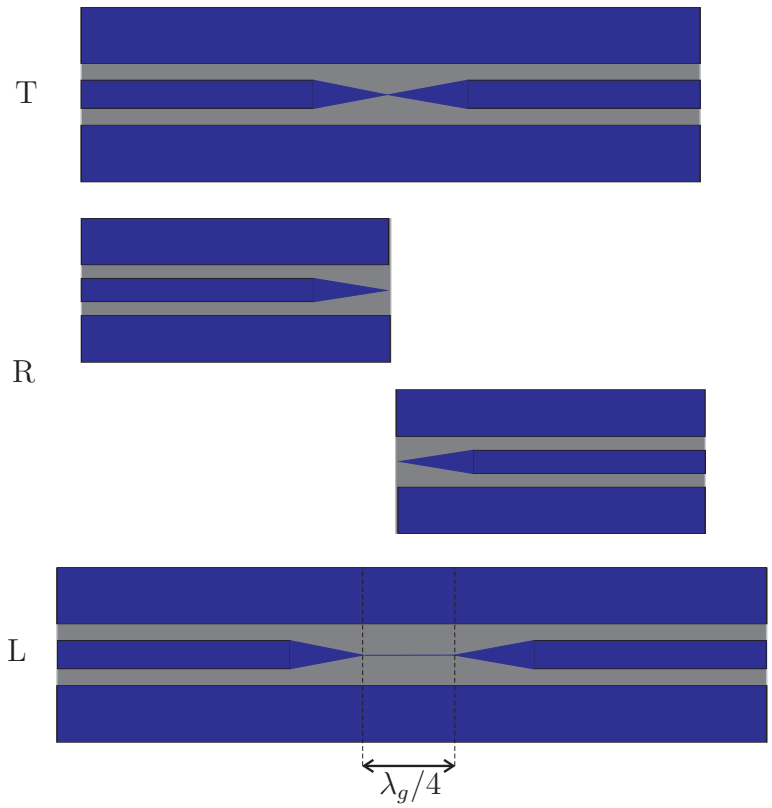

(a)

Figure 3.5 Illustration showing the three TRL structures : THRU, REFLECT, and LINE, respectively.

metal electrodes prior to CNT deposition or growth [30; 31]. Dielectrophoresis is widely used to achieve higher connectivity yields [56]. However, the bottom contact method presents one critically negative aspect : a high contact resistance. Especially for transport experiments, the contact resistance needs to be minimized in order to decrease the reflection at the interface. Due to this, we use a top contact by depositing the tubes first and then evaporating the metal thereby achieving a much better contact to the tube [57].

3.3 Fabrication procedure

3.3.1 CNT deposition and alignment

CNTs used for this work were produced by laser ablation at the *Steacie Institute for Molecular Sciences at the National Research Council of Canada*. The average diameter is 1.1-1.4 nm which yields well-defined characteristics. After filtration, sonication and centrifugation, all of which work on separating the CNTs from the amorphous carbon and other impurities, the average length of a CNT becomes 2 μm. Carbon nanotubes were initially present

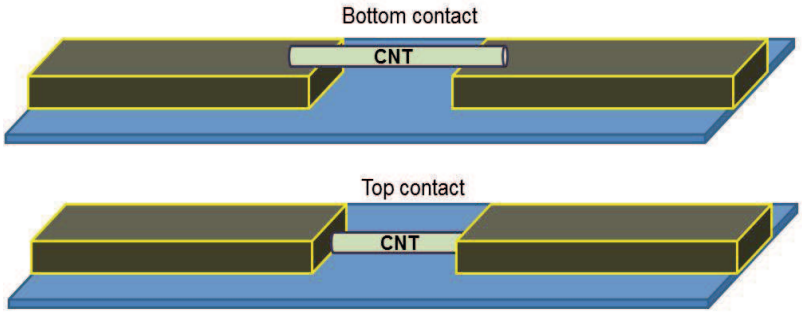

(a)

Figure 3.6 Methods for contacting the CNT : bottom contact or top contact

in a suspension solution (dimethylformamide, Aldrich) at 0.1 mg/ml after sonication treatments. The deposition and assembly of CNTs has been shown to be significantly improved on amine-functionalized surfaces[57]. The substrates were first cleaned by acetone sonication and then were subject to a piranha treatment which cleaned the substrates from organics and in addition attached -OH groups on the surface of the oxide which are necessary for the functionalization step. This latter step evaporates a monolayer of (3-aminopropyl)triethoxysilane (APTES) on top of the silicon susbtrate. The susbtrates were then put in a vacuum furnace for 30 mins [57].
The carbon nanotube deposition method used is based on the well known technique of spin-coating. During which, the susbtrates are placed on a rotating holder (around 3000 rpm) while a drop of the CNT-containing DMF solution is dropped. Due to the centrifugal acceleration, the nanotubes tend to align radially. In order to improve the spread of the solution, another drop of DCE solution is dropped straight after [57]. The density of the nanotubes can be controlled by the number of drops. In order to characterize the deposition, we use the atomic force microscope (AFM). Unlike optical microscopes, the AFM feels the topology of the surface and has a very accurate vertical displacement of 0.5 Å.

In Fig. 3.7, we present typical AFM results on deposited samples. As expected, we noticed increasingly better alignment the further away we probe from the deposition center. It is at these spots where we evaporate the metallic structure and probe through SEM for a connected CNT.

3.3.2 Lithography and lift off

The substrate used was high resistivity intrinsic silicon. The evaporated metal which formed the CPW electrodes was Ti/Cu/Au with thicknesses 15/200/35 nm respectively. Patterning the CPW electrodes is done through a standard photolithography followed by lift-off.

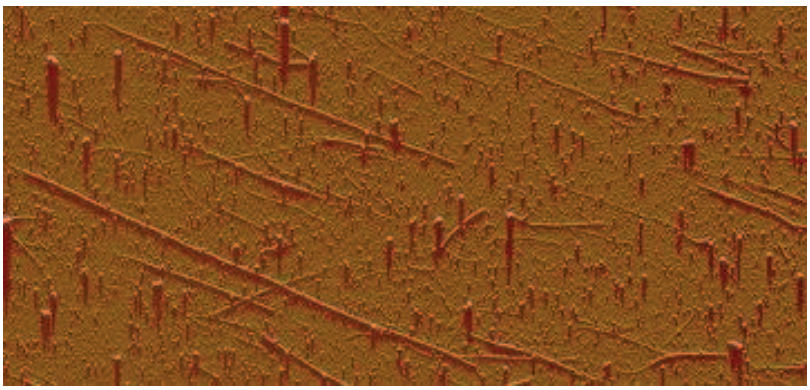

(a)

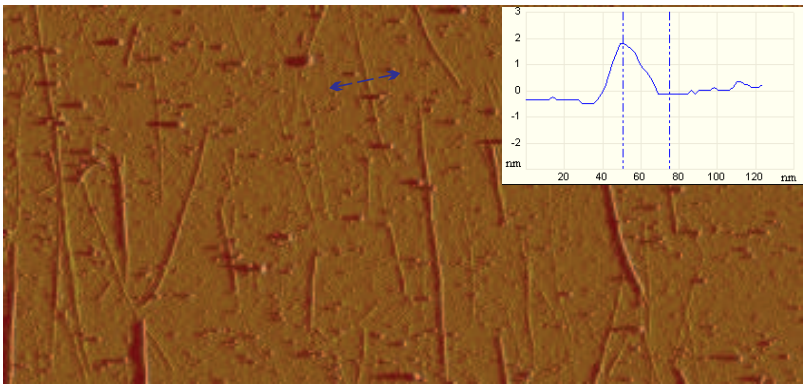

(b)

Figure 3.7 AFM results after spin-coating : (a) and (b) were measured on the same substrate at different locations with respect to the center where the CNTs are dropped. Inset in (b) shows the vertical displacement of the AFM tip corresponding to the diameter of the CNT. Width of the figures correspond to 5 μm.

Briefly, the method consists on evaporating metal across the surface and lift-off the undesired areas. In specific, the first step is to coat the substrate's surface with 2 layers of resist. The bottom of which reacts heavily with a remover that will be used in the lift-off stage. The uppermost layer is a positive photosensitive resist, which simply means that the parts of it exposed to ultra-violet light will be easily removed by the subsequent application of the developer. Since CNTs are chemically inert, all lithography steps are achievable without damaging the tubes in any way. Furthermore, through Reactive Ion Etching (RIE), unwanted nanotubes can be etched from locally specific areas on the substrate.

In our experiments a total 1.5 μm of resist was spin-coated on the surface at 4000 rpm for 30 s. Exposure of the surface with ultraviolet light through the transparent areas of the mask was done for 7 secs at 365 nm wavelength. After exposure, metal was deposited on the

surface using electron-beam evaporation at the LMF facilities of École Polytechnique. 15 nm of titanium were deposited at the bottom as an adherence layer and also due to its high work function that forms a good contact with CNTs. 200 nm of copper was chosen to form the bulk part of the metal due to its high conductivity and low cost. Finally, 35 nm of gold were evaporated on top to avoid oxidation of the copper. Lift off was subsequently achieved by dropping the substrate in a remover bath for an hour. The results of the lithography can be seen in Fig. 3.8 using a regular microscope. As shown, the lithography process was properly optimized and the gap was correctly patterned.

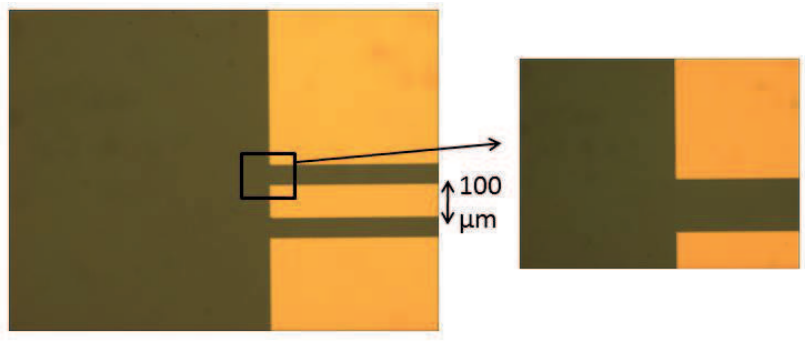

(a)

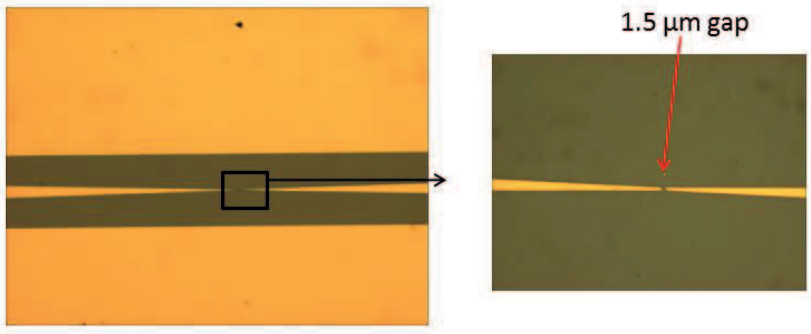

(b)

Figure 3.8 Lithography results : (a) shows the lithography at the edges and (b) shows the tapering of the signal line and the patterning of the gap.

A scanning electron microscope (SEM) was used in order to check for a CNT connection along the gap of the CPWs (each sample contained 10 CPWs at least). The advantage of the SEM over AFM lies in its fast scanning over large areas of the substrates, making it feasible to quickly scan the gaps of the each CPW for a connection. Figure 3.9 shows some of the images in which the connection using CNTs was successfully achieved.

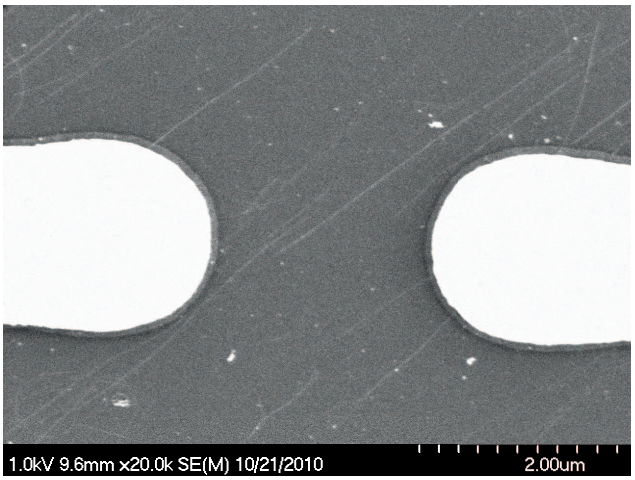

(a)

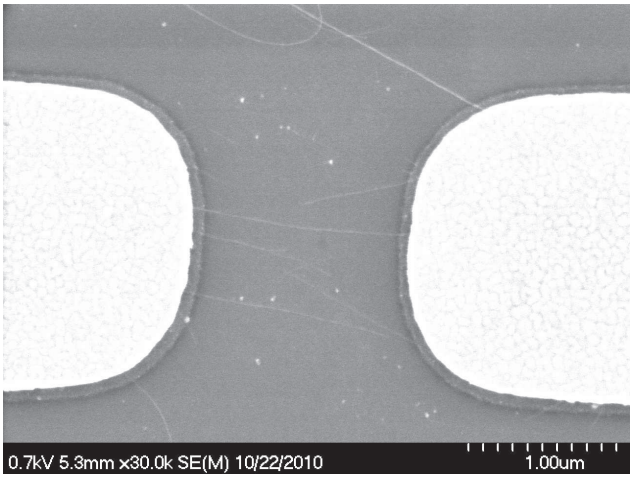

(b)

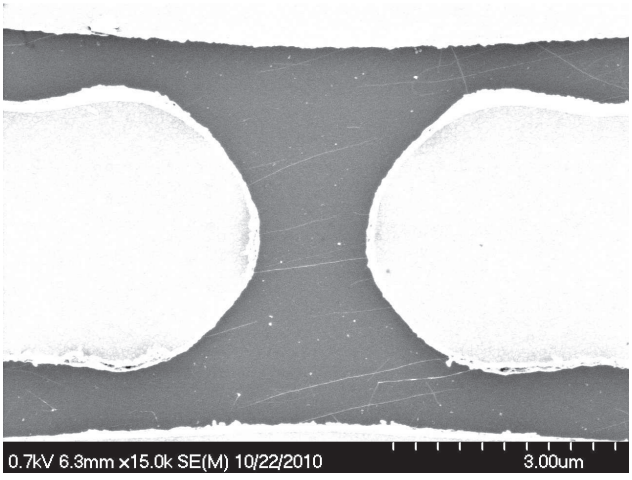

(c)

Figure 3.9 Some of the SEM pictures highlighting : (a) the alignment, (b) and (c) the connection of individual CNTs across the CPW gaps.

3.4 Conclusion

In conclusion, we have fabricated an RF characterization fixture capable of probing the electromagnetic propagation and wave guiding properties of carbon nanotubes up to the THz regime. The upper contact technique that was used guarantees a good contact because the metallic molecules are evaporated on to the substrate and thereby achieving a contact by adhering around the CNT's circumference. Possibly the only disadvantage of this technique relates to lower connectivity yield in comparison with dielectrophoresis [56]. However, with improved CNT deposition techniques, higher yields along with better connections can be achieved in the near future.

CHAPTER 4

Conclusion

4.1 Summary and contributions

The primary objectives of this thesis were to theoretically investigate traveling-wave amplification in m-CNTs, and to fabricate the characterization fixture that could put the theory to the test. Separated into theoretical and fabrication aspects, our main results can be summerized as follows :

Theoretical aspect : We have solved the problem of RF traveling-wave propagation along m-CNTs biased with a DC field. For this purpose, we had to couple the transport and electromagnetic problems by solving the BTE and Maxwell's equations, respectively. Using a linear approximation of the dispersion equation, and neglecting spatial dispersion, an analytical solution for the total current density with respect to the applied fields was found. The analytical solution agreed well with the numerically calculated results. Then, by coupling the BTE with Maxwell's equations the dispersion relation for the surface electromagnetic waves was found using Muller's root finding method. Slow wave propagation, which was previously reported, was found for AC propagation in the absence of a DC field. By comparing with the solution of surface-wave propagation along a copper wire, the large slow-wave factor was shown to be due to the small radius and infinitesimal wall thickness in CNTs. Biasing the m-CNT with a DC field strongly altered the dispersion of the surface waves, increasing both β and α with an increase in E_z^{dc}. However, beyond a DC field of 3×10^5 V/m, the attenuation factor changes sign and the traveling-waves become thus amplifying (Fig. 2.11). Finally, a preliminary treatment which included spatial dispersion resulted in hints of amplification at much lower bias, namely $E_z^{dc} = 10^4$ V/m (Fig. 2.15). Such results could have important implications and are deemed worthy of further investigations.

In retrospect, the main contributions of the theoretical solution include :

1. An AC-DC solution of the BTE-RTA for a m-CNT using the tight-binding dispersion
2. An analytical solution of the AC current density, neglecting spatial dispersion, in a m-CNT biased by a DC field.
3. A calculated negative AC conductivity with beyond a threshold E_z^{dc}.
4. Amplification of the traveling-waves beyond $E_z^{dc} = 3 \times 10^5$ V/m was calculated when spatial dispersion is assumed negligible. This amplification was shown not to be TWT-

like due to a mismatch between phase and drift velocities at this threshold field. Bloch-type phenomenon was concluded to be the physical mechanism behind such amplification.

5. Amplification of the traveling-waves beyond $E_z^{dc} = 10^4$ V/m was calculated when spatial dispersion is included, coinciding with a match between the phase and drift velocities. Thereby implying a possible TWT-like amplification.

Fabrication aspect : We have designed and fabricated an RF characterization fixture that could test the theoretical results. We chose the CPW due to its versatility and robustness for high-frequency measurements. The CPW was designed so that the signal trace is tapered to only 2 μm wide, and a 1.5 μm gap allowed the CNTs to be aligned for measurements. The CNTs were deposited on the substrates as a first step, using spin-coating which aligned the CNTs radially. Using the AFM, we characterized the deposition to the desired concentration and alignment. Afterwards, we patterned the designed CPW waveguides using standard optical lithography/lift-off. After this final step, alignment across the CPW gaps was probed using the SEM. Successful contacts was achieving in many instances by a single or multiple CNTs.

4.2 Limitations and future improvements

Theoretical aspect : The BTE was solved assuming the RTA which is accurate at low-fields but provides at most a qualitative picture for higher fields. The main limitation of RTA is that it assumes energy-independent scattering time. Therefore, in future work, the model can be improved by using an energy-dependent scattering time which takes into account the optical phonons at high bias. Furthermore, in most of the analysis, we assumed spatially local fields (ie. we neglected spatial dispersion), which is reasonable as a first approximation. A crude initial calculation including spatial dispersion was finally performed but the absence of a rigorous complex plane analysis leaves the treatment incomplete.

Fabrication aspect : The measurements were not performed and reported in this thesis due to two shortcomings of the design and fabrication :

1. The length of the CPW sections, being greater than the wavelength at the designed frequency band, causes large difficulties in calibration and de-embedding.
2. The CNTs used had a 2 μm mean lengths which are lumped elements at the proposed frequency band.

3. Insufficient oxide layer on the substrate meant that CNTs aligned across the gap were short circuited by the finite resistance of the intrinsic Si.

Therefore, in future fabrication and characterization works, CNTs with greater lengths must be acquired or grown directly on the substrate. On the other hand, shorter CPW sections must excite the CNTs to ensure easier calibration of the measurements.

REFERENCES

[1] C. White and T. N. Todorov, "Carbon nanotubes as long ballistic conductors ," *Nature*, vol. 393, no. 240, 1998.

[2] G. Slepyan, S. Maksimenko, A. Lakhtakia, O. Yevtushenko, and A. Gusakov, "Electrodynamics of carbon nanotubes : dynamic conductivity, impedance boundary conditions, and surface wave propagation," *Physical Review B*, vol. 60, no. 24, pp. 17 136–17 149, 1999.

[3] A. Gilmour, *Principles of Traveling Wave Tubes*. Boston-London : Artech House, 1994.

[4] R. Saito, M. Dresselhaus, and G. Dresselhaus, *Physical Properties of Carbon Nanotubes*. London : Imperial College Press, 1998.

[5] S. Iijima, "Helical microtubules of graphitic carbon," *Nature*, vol. 354, no. 6348, pp. 56–58, 1991.

[6] K. Novososelov, M. S. Geim, A. K., D. Jiang, Y. Zhang, S. Dubonos, I. Grigorieva, and A. Firsov, "Electric field effect in atomically thin carbon films," *Science*, vol. 306, no. 5696, 2004.

[7] C. Kittel, *Solid State Physics*. New Jersey : Wiley, 2005.

[8] R. M. Martin, *Electronic Structure : Basic Theory and Practical Methods*. Cambridge : Cambridge University Press, 2008.

[9] J. Carlo, *Theory of Electrical Transport in Semiconductors*. New York : Springer, 1972.

[10] S. Datta, *Quantum Transort : Atom to Transistor*. Cambridge : Cambridge, 2005.

[11] S. Reich, J. Maultzsch, C. Thomsen, and P. Ordejón, "Tight-binding description of graphene," *Physical Review B*, vol. 66, no. 035412, pp. 1–5, 2002.

[12] J. Mintmire, "Electronic and structural properties of carbon nanotubes," *Carbon*, vol. 33, no. 7, 1995.

[13] J. W. Mintmire and C. T. White, "Universal density of states for carbon nanotubes," *Physical Review Letters*, vol. 81, no. 12, pp. 2506–2509, 1998.

[14] M. P. Anantram and F. Léonard, "Physics of carbon nanotube electronic devices," *Reports on Progress in Physics*, vol. 69, no. 3, pp. 507–561, 2006.

[15] J.-Y. Park, S. Rosenblatt, Y. Yaish, V. Sazonova, H. Üstünel, S. Braig, T. a. Arias, P. W. Brouwer, and P. L. McEuen, "Electronphonon scattering in metallic single-walled carbon nanotubes," *Nano Letters*, vol. 4, no. 3, pp. 517–520, 2004.

[16] J. Kong, E. Yenilmez, T. Tombler, W. Kim, H. Dai, R. Laughlin, L. Liu, C. Jayanthi, and S. Wu, "Quantum interference and ballistic transmission in nanotube electron waveguides," *Physical Review Letters*, vol. 87, no. 10, pp. 1–4, 2001.

[17] Z. Yao, C. Kane, and C. Dekker, "High-field electrical transport in single-wall carbon nanotubes," *Physical Review Letters*, vol. 84, no. 13, pp. 2941–4, 2000.

[18] G. Pennington and N. Goldsman, "Semiclassical transport and phonon scattering of electrons in semiconducting carbon nanotubes," *Physical Review B*, vol. 68, no. 4, pp. 1–11, 2003.

[19] A. Maksimenko and G. Slepyan, "Negative differential conductivity in carbon nanotubes," *Physical Review Letters*, vol. 84, no. 2, 2000.

[20] E. Pop, D. Mann, J. Cao, Q. Wang, K. Goodson, and H. Dai, "Negative differential conductance and hot phonons in suspended nanotube molecular wires," *Physical Review Letters*, vol. 95, no. 155505, pp. 1–4, 2005.

[21] T. Dürkop, S. A. Getty, E. Cobas, and M. S. Fuhrer, "Extraordinary mobility in semiconducting carbon nanotubes," *Nano Letters*, vol. 4, no. 1, pp. 35–39, 2004.

[22] C. Zhou, J. Kong, E. Yenilmez, and H. Dai, "Modulated chemical doping of individual carbon nanotubes," *Science*, vol. 290, no. 5496, 2000.

[23] R. Martel, T. Schmidt, H. R. Shea, T. Hertel, and P. Avouris, "Single- and multi-wall carbon nanotube field-effect transistors," *Applied Physics Letters*, vol. 73, no. 17, pp. 2447–2449, 1998.

[24] R. Martel, V. Derycke, C. Lavoie, J. Appenzeller, K. Chan, J. Tersoff, and P. Avouris, "Ambipolar electrical transport in semiconducting single-wall carbon nanotubes," *Physical Review Letters*, vol. 87, no. 25, pp. 17–20, 2001.

[25] M. W. Bockrath, "Carbon nanotubes : electrons in one dimension," Ph.D. dissertation, University of California - Berkeley, 1999.

[26] P. J. Burke, "Luttinger liquid theory as a model of the gigahertz electrical properties of carbon nanotubes," *IEEE Transactions on Nanotechnology*, vol. 1, no. 3, 2002.

[27] G. Hanson, "Fundamental transmitting properties of carbon nanotube antennas," *IEEE Transactions on Antennas and Propagation*, vol. 53, no. 11, 2005.

[28] Y. Wang, K. Kempa, B. Kimball, J. B. Carlson, G. Benham, W. Z. Li, T. Kempa, J. Rybczynski, A. Herczynski, and Z. F. Ren, "Receiving and transmitting light-like radio waves : Antenna effect in arrays of aligned carbon nanotubes," *Applied Physics Letters*, vol. 85, no. 13, 2004.

[29] L. Gomez-rojas, S. Bhattacharyya, E. Mendoza, D. C. Cox, J. M. Rosolen, and S. R. P. Silva, "RF response of single-walled carbon nanotubes," *Nano letters*, vol. 7, no. 9, pp. 2672–2675, 2007.

[30] M. G. Kang, J. H. Lim, S. H. Hong, D. J. Lee, S. W. Hwang, D. Whang, J. S. Hwang, and D. Ahn, "Microwave characterization of a single wall carbon nanotube bundle," *Japanese Journal of Applied Physics*, vol. 47, no. No. 6, pp. 4965–4968, 2008.

[31] J. J. Plombon, K. P. O'brien, F. Gstrein, V. M. Dubin, and Y. Jiao, "High-frequency electrical properties of individual and bundled carbon nanotubes," *Journal of Applied Physics*, vol. 90, no. 063106, 2007.

[32] A. Kis and A. Zettl, "Nanomechanics of carbon nanotubes." *Philosophical Transactions of the Royal Society A*, vol. 366, pp. 1591–611, 2008.

[33] P. Poncharal, Z. Wang, D. Ugarte, and de Heer Walt, "Electrostatic deflections and electromechanical resonances of carbon nanotubes," *Science*, vol. 283, no. 5407, pp. 1513–6, 1999.

[34] E. W. Wong, "Nanobeam mechanics : Elasticity, strength, and toughness of nanorods and nanotubes," *Science*, vol. 277, no. 5334, pp. 1971–1975, 1997.

[35] J. Charlier and J. Michenaud, "Energetics of multilayered carbon tubules," *Physical Review Letters*, vol. 70, no. 12, pp. 1858–1861, 1993.

[36] A. M. Fennimore, T. D. Yuzvinsky, W.-q. Han, M. S. Fuhrer, J. Cumings, and A. Zettl, "Rotational actuators based on carbon nanotubes," *Nature*, vol. 424, no. July, pp. 408–410, 2003.

[37] T. Rueckes, K. Kim, E. Joselevich, G. Tseng, C. Cheung, and C. Lieber, "Carbon nanotube-based nonvolatile random access memory for molecular computing," *Science*, vol. 289, no. 5476, pp. 94–7, 2000.

[38] J. Cumings and A. Zettl, "Low-friction nanoscale linear bearing realized from multiwall carbon nanotubes," *Science*, vol. 289, no. 5479, pp. 602–4, 2000.

[39] H. Peng, C. Chang, S. Aloni, T. Yuzvinsky, and A. Zettl, "Ultrahigh frequency nanotube resonators," *Physical Review Letters*, vol. 97, no. 087203, pp. 2–5, 2006.

[40] G. Slepyan, S. Maksimenko, A. Lakhtakia, O. Yevtushenko, and A. Gusakov, "Electronic and electromagnetic properties of nanotubes," *Physical Review B*, vol. 57, no. 16, pp. 9485–9497, 1998.

[41] M. Lundstrom, *Fundamentals of Carrier Transport*, 2nd ed. Cambridge : Cambridge University Press, 2000.

[42] B. B. G. and R. Engelmann, *Gunn-Effect Electronics*. New York : John Wiley Sons, 1975.

[43] S. Tans, M. H. Devoret, H. Dai, A. Thess, R. E. Smalley, L. J. Geerligs, and C. Dekker, "Individual single-wall carbon nanotubes as quantum wires," *Nature*, vol. 386, no. 474, 1997.

[44] J.C. Vaissiere, J.P. Nougier, L. Varani and P. Houlet, "Small signal analysis of the Boltzmann equation from harmonic and impulse response methods," *Physical Review B*, vol. 49, no. 16, pp. 11 144–11 152, 1994.

[45] W. Boyce and R. DiPrima, *Elementary Differential Equations and Boundary Value Problems*. New York : John Wiley, 2001.

[46] L. Esaki and R. Tsu, "Superlattice and negative differential conductivity in semiconductors," *IBM Journal of Research and Developpement*, pp. 61–65, 1970.

[47] J. A. Stratton, *Electromagnetic Theory*. New York : John Wiley Sons, 2007.

[48] R. F. Harrington, *Time-Harmonic Electromagnetic Fields*. Hoboken : Wiley-IEEE Press, 2001.

[49] A. Sommerfeld, "Fortpflanzung elektrodynamischer wellen an einem zylindrischen leiter," *Annalen der Physik und Chemie*, vol. 233, 1899.

[50] G. Goubau, "Surface Waves and Their Application to Transmission Lines," *Journal of Applied Physics*, vol. 21, 1950.

[51] F. Bloch, "Uber die quantenmechanik der elektronen in Kristallgittern," *Z. Phys.*, vol. 52, no. 7-8, 1928.

[52] S. Ktitorov, G. Simin, and V. Sindalovskii, "Bragg reflections and the high-frequency conductivity of an electronic solid-state plasma," *Fizika Tverdogo Tela*, vol. 13, 1972.

[53] X. Zhou, J.-Y. Park, S. Huang, J. Liu, and P. McEuen, "Band structure, phonon scattering, and the performance limit of single-walled carbon nanotube transistors," *Physical Review Letters*, vol. 95, no. 146805, 2005.

[54] I. Wolff, *Coplanar Waveguide Integrated Circuits*. New Jersey : John Wiley and Sons, 2008.

[55] R. Marks, "A multiline method of network analyzer calibration," *IEEE Transactions on Microwave Theory and Techniques*, vol. 39, no. 7, 1991.

[56] A. Vijayaraghavan, S. Blatt, D. Weissenberger, M. Oron-carl, F. Hennrich, D. Gerthsen, H. Hahn, and R. Krupke, "Ultra-Large-Scale Directed Assembly of Single-Walled Carbon Nanotube Devices," *Nano Letters*, vol. 7, no. 6, 2007.

[57] C. Aguirre, "Carbon nanotubes networks for thin film organic electronic applications," Ph.D. dissertation, Université de Montréal, 2007.

ANNEXE A

Surface Wave Mode (TM_z) for a Full Cylindrical Conductor

The surface wave mode along a conducting cylinder was first derived by Sommerfeld [49]. The mode propagating along such a structure is a TM_z mode with a relatively low attenuation constant. Goubau later used this single cylindrical wire as a transmission line, exciting the mode using a horn antenna [50]. For a cylindrical conductor with azimuthal symmetry, the field components of the traveling-wave mode are,

$$\mathbf{E}_{\rho}^{\mathbf{ac}} = \hat{\rho} e^{j(hz-\omega t)} \begin{cases} jA\frac{h}{\gamma_c} J_1(\gamma_c \rho) & \text{for } \rho < R \\ jA\frac{h}{\gamma} H_1(\gamma \rho) & \text{for } \rho > R \end{cases}, \tag{A.1}$$

$$\mathbf{E}_{\mathbf{z}}^{\mathbf{ac}} = \hat{z} e^{j(hz-\omega t)} \begin{cases} jA J_0(\gamma_c \rho) & \text{for } \rho < R \\ jA H_0(\gamma \rho) & \text{for } \rho > R \end{cases}, \tag{A.2}$$

$$\mathbf{H}_{\phi}^{\mathbf{ac}} = \hat{\phi} e^{j(hz-\omega t)} \begin{cases} jA\frac{k_c^2}{\omega \mu_c \gamma_c} J_1(\gamma_c \rho) & \text{for } \rho < R \\ jA\frac{k^2}{\omega \mu \gamma} H_1(\gamma \rho) & \text{for } \rho > R \end{cases}, \tag{A.3}$$

where h is the axial wavenumber, A is the amplitude, γ is the transverse wavenumber, k is the free space wavenumber, $J(\cdot)$ and $H(\cdot)$ are the Bessel and Hankel functions of the first kind respectively, and R is the radius of the cylinder. The subscript 'c' refers to wavenumber values within the conductor material. The wavenumbers are related through

$$h^2 = \gamma_c^2 + k_c^2, \quad \text{and} \quad h^2 = \gamma^2 + k^2, \tag{A.4}$$

where $k_c = \sqrt{\omega \mu_c \sigma_c}$ with μ and σ being the permeability and conductivity, respectively. In this section, we consider a bulk material with known frequency-independent conductivity, therefore k_c is known with respect to frequency.

Applying the boundary conditions which ensure the continuity of the tangential electric and magnetic fields yields

$$\frac{\mu}{\mu_c} \frac{\gamma}{\gamma_c} \frac{k_c^2}{k^2} \frac{H_0(\gamma R) J_1(\gamma_c R)}{H_1(\gamma R) J_0(\gamma_c R)} = 1. \tag{A.5}$$

The determinantal equation is solved for a copper wire with various radii using Muller's method which yields the frequency dispersion of the surface mode and consequently its phase velocity, shown respectively in fig. A.1 and A.2.

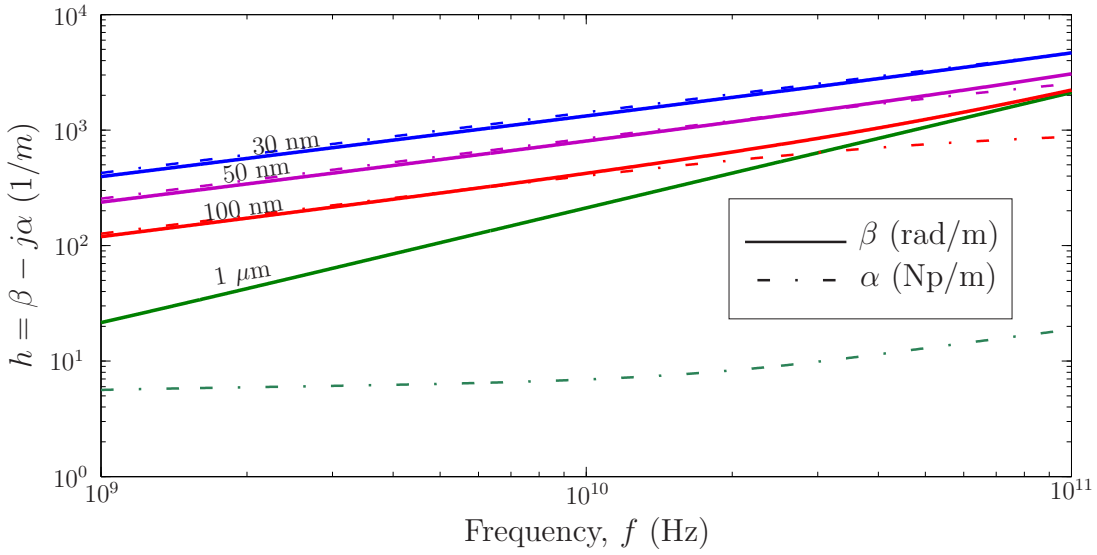

Figure A.1 Electromagnetic dispersion relation $h(\omega) = \beta(\omega) - j\alpha(\omega)$ (2.41) of a copper conductor found by solving (A.5).

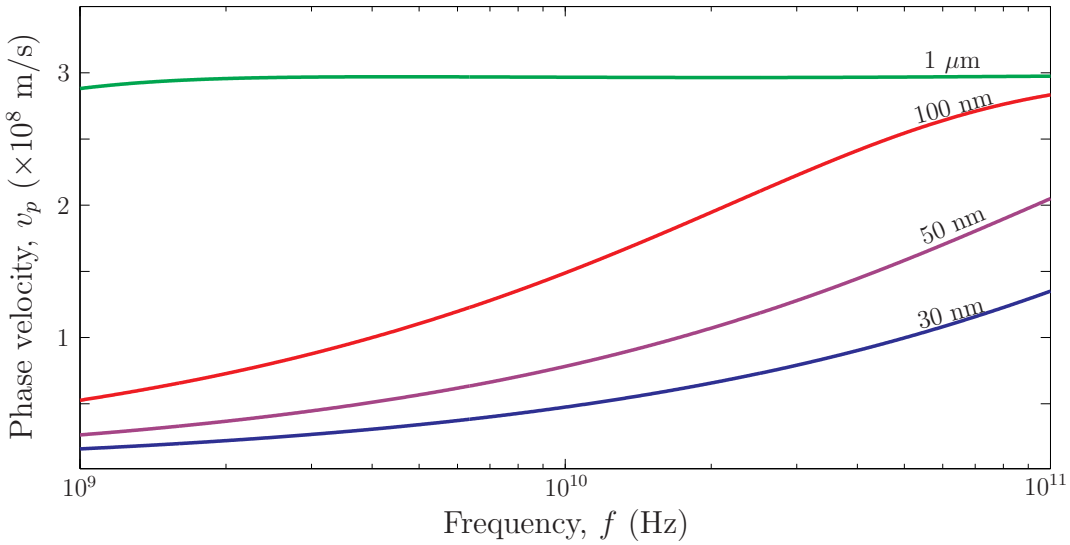

Figure A.2 Phase velocity of the surface-wave modes plotted in fig. A.1 for various radii. A substantial decrease in the phase velocity is found for a radius smaller than 1 μm.